RSC Advances

PAPER

View Article Online
View Journal | View Issue

Cite this: *RSC Adv.*, 2025, **15**, 15651

Enhanced photocatalytic activity of SnO_2@g-C_3N_4 heterojunctions for methylene blue and bisphenol-A degradation: effect of interface structure and porous nature†

Vaibhav Salve,[a] Pramod Agale,[a] Sagar Balgude,[b] Satish Mardikar,[c] Sonaba Dhotre[d] and Paresh More *[a]

In this study, SnO_2@graphitic carbon nitride (g-C_3N_4) heterojunctions were synthesized using a hydrothermal method followed by sonication. The catalytic efficiency of SnO_2@g-C_3N_4 under sunlight was evaluated for methylene blue (MB) and bisphenol A (BPA) degradation. Characterization techniques, including X-ray diffraction (XRD), field emission scanning electron microscopy (FESEM), and high-resolution transmission electron microscopy (HRTEM), confirmed the successful formation of SnO_2 nanoparticles on g-C_3N_4 (GCN) sheets with porous morphology. The SnO_2@GCN heterojunction achieved a 97% degradation efficiency for MB in 45 minutes, outperforming pure SnO_2 (65.3%) and g-C_3N_4 (73.8%). Thus, the increase in photocatalytic activity is due to an enhancement in charge separation and an increase in the absorption of sunlight. For BPA degradation, the 5.0% SnO_2@GCN composite demonstrated approximately 99% efficiency within 60 minutes. Additionally, recyclability tests showed good stability after five cycles, with no significant structural changes confirmed by FTIR and FESEM analyses. This study highlights the importance of interface structure and porous morphology in enhancing photocatalytic efficiency, paving the way for effective photocatalysts for wastewater treatment applications.

Received 11th March 2025
Accepted 29th April 2025

DOI: 10.1039/d5ra01762a

rsc.li/rsc-advances

1. Introduction

The environment is rapidly deteriorating due to industrial effluents, particularly from the textile, dye, pharmaceutical, and chemical sectors. These effluents, especially those containing dyes, are not only visually displeasing but also severely impact marine ecosystems.[1,2] In the dyeing process, a significant amount of dye is discharged into water bodies, resulting in carcinogenic and mutagenic effects.[3,4] Traditional wastewater treatment methods, including adsorption, chemical coagulation, and advanced oxidation, have limitations, especially in removing the dyes completely from the effluents. Therefore, managing industrial waste has become a formidable challenge.[5,6]

Recent studies have highlighted the potential of nanomaterials in improving wastewater treatment, particularly for dye degradation. Research on metal oxides and ferrites has demonstrated their effectiveness in photodegrading pollutants.[5,6] For instance, our group previously reported the photodegradation of methylene blue (MB) using Sr-doped ZnO nano-disks within 60 minutes[7] and the catalytic adsorption efficiency of a Co_3O_4@-MWCNT composite, which degraded Coracryl dye in just 4 minutes and reduced 4-nitrophenol in 7 minutes.[8] The very high activity was attributed to the structural properties of nanomaterials, including their high surface area and crystallinity.

Recently, researchers have integrated covalent organic frameworks (COFs) with inorganic materials to synthesize composite materials. These synthesized composites have been found to be highly functionalized materials with a very high surface area. The heterostructure between COFs and inorganic materials (inorganic–organic heterostructure) is responsible for novel properties of COF-based nanocomposites.[9,10]

Carbon-based materials have enormous applications in CO_2 reduction[11] as well as in aniline elimination.[12] Materials such as multi-walled carbon nanotubes (MWCNTs) have also been widely studied because of their superior porosity and high surface area, which enhance photocatalytic efficiency.[13–15] Composites, such as Ag nanoparticles on activated carbon, ZnO/CSAC, and Ag–TiO_2/GNSAC, have shown improved catalytic activities over various dyes compared to their pristine forms.[13–15] Among emerging photocatalysts, graphitic carbon nitride (g-

[a]*Department of Chemistry, K. E. T's, Vinayak Ganesh Vaze College Autonomous, Mulund, Mumbai, Maharashtra, 400081, India. E-mail: paresh.m34@gmail.com*
[b]*Department of Chemistry, MES Abasaheb Garware College, Karve Road, Pune, Maharashtra, 411004, India*
[c]*Department of Chemistry, SRS College, SGB Amravati University, Amravati, Maharashtra, India*
[d]*Department of Chemistry, PDEA's Prof. Ramkrishna More College, Akurdi, Pune, Maharashtra, India*

† Electronic supplementary information (ESI) available. See DOI: https://doi.org/10.1039/d5ra01762a

C_3N_4) has attracted attention due to its tuneable properties.[16] However, the recombination of charge carriers limits its performance.[17–21] To address this, researchers have explored composite materials to suppress recombination and enhance photocatalytic activity.[17–21]

Heterojunctions between g-C_3N_4/DE/Ag/AgCl/CNDE display outstanding photocatalytic activity in highly carcinogenic Cr^{+6} reduction and in MB dye degradation.[22,23] Further, many studies on the interface between g-C_3N_4 and metal oxides, such as ZnO, SnO_2 and Fe_3O_4, have been widely reported.[24–26] Among these, SnO_2@g-C_3N_4 stands out due to its favourable band gap alignment, which promotes effective charge separation and enhances photocatalytic efficiency.[27–29] The band gap difference between SnO_2 (3.6–3.8 eV) and g-C_3N_4 (2.7–2.8 eV) supports the formation of a heterojunction, further improving performance.[27–29] Previous studies, such as those by Praus and Akhundi, have demonstrated enhanced photodegradation of rhodamine B using SnO_2@g-C_3N_4 composites.[30,31] However, a more in-depth exploration of this material is needed, particularly for practical applications in dye degradation and environmental remediation.

Our current work focuses on developing a SnO_2@g-C_3N_4 nanocomposite *via* the hydrothermal method, aiming to enhance the photodegradation of pollutants like MB dye and BPA. The novelty of our approach lies in the utilization of heterojunctions and porous structures to improve charge transfer and separation at the catalyst interface, which is distinct from the adsorption mechanisms seen in previous studies, such as those involving Co_3O_4@MWCNT and Sr-doped ZnO.[7,8] In contrast to the extensively studied TiO_2@g-C_3N_4, research on SnO_2@g-C_3N_4 remains limited despite its promising potential for enhanced photocatalytic activity due to superior charge separation and higher reduction potential.[31]

In addition to MB degradation, our study is extended to the removal of BPA, a persistent organic pollutant widely used in polymer production. BPA poses significant risks to human health and ecosystems, with known endocrine-disrupting effects and environmental persistence.[32–36] Although various treatment methods exist, there remains a need for more efficient, cost-effective solutions.[37] Our work aims to fill this gap by demonstrating the efficacy of SnO_2@g-C_3N_4 for the photodegradation of both MB and BPA, establishing a robust method for tackling complex environmental pollutants.

This study presents a novel approach by synthesizing SnO_2@g-C_3N_4 nanocomposites and highlights their potential for improved photocatalytic performance in wastewater treatment applications. Characterization techniques such as FTIR, XRD, FESEM, EDS, TEM, XPS, RAMAN, and UV-vis spectroscopy were employed to confirm the material properties and catalytic performance of the synthesized composite, setting the stage for further advancements in environmental remediation.

2. Experimental

2.1 Materials

Stannic chloride pentahydrate ($SnCl_4 \cdot 5H_2O$) was purchased from Research Laboratories (RL), Mumbai, Maharashtra. Melamine ($C_3H_6N_6$), trisodium citrate dihydrate ($Na_3C_6H_5O_7$), PEG-200 and sodium hydroxide (NaOH) were purchased from Loba Chemicals Mumbai, Maharashtra and were used as received. The chemicals used in the synthesis of the catalyst obtained from RL and Loba Chemicals Mumbai were of 99% purity.

2.2. Synthesis of SnO_2@g-C_3N_4 nanocomposite

2.2.1. Synthesis of SnO_2. 7.0 g of $SnCl_4 \cdot 5H_2O$, 8.82 g of sodium citrate and 25 mL PEG-200 were added to 25 mL of distilled water. The solution obtained was continuously stirred for homogeneity, followed by a dropwise addition of 25 mL ethanol. 50 mL of 2 M NaOH was added dropwise in this homogeneous solution with constant stirring, followed by sonication for 30 min. After sonication, the solution was transferred to a hydrothermal reactor and heated to 120 °C for 12 h. The synthesized product was washed several times with deionised water using a centrifuge machine (5000 rpm). The product was dried in an oven at 80 °C for 8 h to obtain SnO_2 and labelled as SnO_2.

2.2.2. Synthesis of g-C_3N_4 (GCN). The pristine g-C_3N_4 was prepared from melamine. 5 g of melamine was weighed, transferred in the silica crucible and fired in the furnace at 550 °C for 4 h. It resulted in a yellow coloured product, which was ground with a mortar and pestle and labelled GCN.

2.2.3. Synthesis of SnO_2@g-C_3N_4 nanocomposite. 2.5 wt% SnO_2@GCN nanocomposite was synthesized using 0.025 g of GCN dispersed in ethanol and sonicated in 50 mL ethanol. After ultra-sonic treatment for 1 h, a certain amount of pristine SnO_2 nanomaterial was added into a beaker containing 50 mL ethanol. Both the solutions were mixed, ultrasonically dispersed for 30 min. And filtered. The product obtained was fired in an oven for 6 h. At a temperature of 80 °C. The prepared sample was named as 2.5% SnO_2@GCN. For the preparation of different concentrations of SnO_2@GCN (5.0 wt%, 7.5 wt%, and 10 wt%) nanocomposites, different weights of the as-synthesized GCN (0.05 g, 0.075 g, and 0.10 g) were taken, and the remaining steps of the preparation remained the same as above. The compounds synthesized were labelled as 5.0% SnO_2@GCN, 7.5% SnO_2@GCN and 10.0% SnO_2@GCN, respectively.

2.3. Characterization

The Rigaku X-ray diffractometer with Cu kα radiation (λ = 1.5418 Å), power source of 40 kV, current of 40 mA, NIST 1976b corundum standard with the sampling parameters (start angle-5° to 90°) was used to obtain the XRD of samples. FTIR spectra within the 400 to 4000 cm^{-1} wavenumber range were recorded with a 3000 Hyperion Microscope with vertex 80 FTIR spectrometer. The source used was SiC, also called the Globar source, with a power of 50–100 mW. The instrument was calibrated using polystyrene standard, which is in-built. The baseline was corrected manually, and the number of scans was −32 scans with the scanned resolutions of 4 cm^{-1}. The morphology and microstructure of the compounds were recorded on Carl Zeiss, model Supra 55. The source used was LaB6 with an

accelerating voltage of 0.1 to 30 kV and vacuum pressure of −2–133 Pa under the probe current −4 pA–10 nA. The detector used was Everhart Thornley Secondary Electron Detectors with the magnification −79 to 1 000 00×. Further, transmission electron microscopy (TEM, JEOL JEM 2100) with LaB6 source, 200 kV power, and accelerating voltage of 20 to 200 kV was used to study the morphology of samples. The instrument was calibrated using a gold lattice as a standard grid. Oxidation states and elements were confirmed using XPS on Thermo Fischer Scientific ESCALAB Xi+ (Source aluminium *k* alpha radiation energy). The voltage applied was 1486.7 eV with a carbon standard peak at 284.8 eV, pass energy for survey of 50 eV and pass energy for short scan of 20 eV. The scanning resolution was 0.03 eV with a vacuum level 5.2×10^{-10} mb analyser. Hemisphere having argus mean radius of 124 mm. The angle between the analyser to the source was 90° with an instrument resolution of 0.60 eV. The band gap of all the samples was recorded on a UV-visible spectrophotometer (Shimadzu Model UV-2700). A surface area analyser (St 1 on NOVA touch 1LX) was used to calculate the surface area of the samples. Raman spectral analysis was carried out using a Renishaw spectrophotometer. Lasers used in the instrument are of high power near IR diode laser with 300 mW at 785 nm (air cooled). The standard used was silicone with an integral narrow bandpass filter having external mounting on a laser kinematic baseplate. Photocurrent and EIS studies were conducted using an impedance analyser (NOVA FRA2 μ Auto lab type III (μ3Au771301)). The photodegradation of MB dye was studied on a UV-visible spectrophotometer (Shimadzu model 1800). Degradation of BPA was studied using high-performance liquid chromatography (HPLC), using a Hitachi Primaide 1120-system liquid chromatograph (Hitachi®, Palo Alto, CA) equipped with a quaternary high-pressure pump (1110 series), a single wavelength UV detector (1410 series), and an autosampler (1210 series). Data analysis was carried out using Hitachi Chem Station software.

2.4. Electrochemical measurements

Electrochemical measurements such as photocurrent and electrochemical impedance spectroscopy (EIS) were performed using a three-electrode system. The system consists of platinum as the counter electrode, Hg/Hg_2Cl_2 electrode as the reference electrode and the as-synthesized catalyst as the working electrode. The working electrode consists of 80 wt% of the active material, 10 wt% activated carbon (conducting additive) and 10 wt% of polyvinyl difluorides (PVDF). These three materials were mixed in a *N*-methyl pyrrolidone (NMP) solvent, ground in a mortar and pestle, and using a doctor blade method, it was coated on 1 × 3 cm indium–tin oxide (ITO) glass and dried at 70 °C for 5–6 h. Photocurrent and EIS studies were conducted using sodium sulphate solution (Na_2SO_4) as an electrolyte.

2.5 Photocatalytic activity evaluation

The MB dye was degraded over the samples (SnO_2, 2.5% SnO_2@GCN, 5.0% SnO_2@GCN, 7.5% SnO_2@GCN and 10.0% SnO_2@GCN). In a 100 mL MB solution of 100 ppm concentration, 10 mg of the catalyst was added and sonicated for 5 minutes. The absorption/desorption experiment was carried out for half an hour in dark conditions so that the dye molecules were in equilibrium with the catalyst. In regular intervals of 5 min, the dye solution was removed and its photodegradation was studied at 663 nm using a UV-visible spectrophotometer. The discoloration of the dye was judged at the maximum absorption wavelength.

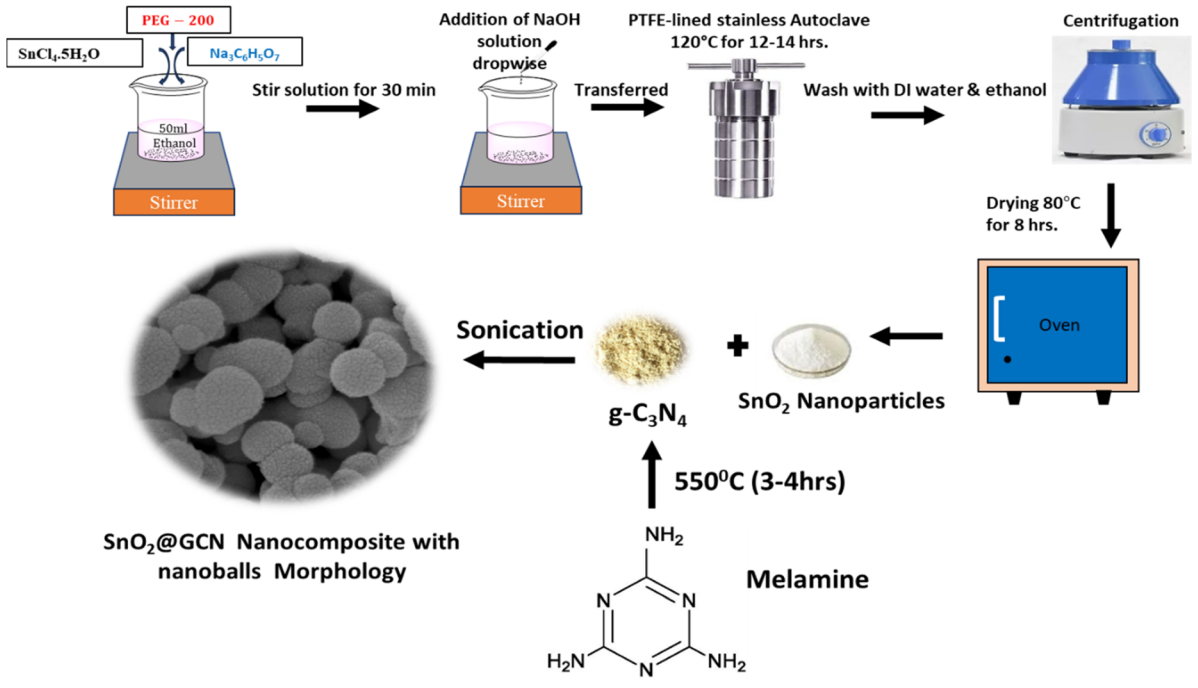

Scheme 1 Schematic illustration of the synthesis of SnO_2@GCN nanocomposites.

The as-synthesized pristine SnO_2 and SnO_2@GCN photocatalysts were also tested for the photodegradation of BPA under sunlight irradiation. Prior to photodegradation, the photocatalyst (35 mg) was added to the BPA solution (50 mL) and the suspension was sonicated for 2 min, followed by magnetic stirring in the dark for 30 min in order to reach the adsorption–desorption equilibrium. During photodegradation, after regular time intervals, ~1.0 mL solution was withdrawn and filtered through a PTFE filter to remove the catalyst. The residual BPA concentration was analysed using HPLC with water/methanol (30/70, v/v) as a mobile phase (Scheme 1).

The limitation of this study is that during experimentation, conclusions were drawn based on a single data set collected. Even the data set collected does not include ESD (Estimated Standard Deviation); hence, the error values were not determined.

3. Results and discussion

The crystal structures of GCN, SnO_2 nanoparticles and SnO_2@GCN (2.5%, 5.0%, 7.5% and 10.0%) nanocomposites were investigated using XRD (Fig. 1a). Fig. 1a shows five distinct diffraction peaks at (110), (101), (200), (211), and (301) planes, corresponding to the tetragonal rutile structure of SnO_2 (JCPDS Card No. 41-1445) and SnO_2@GCN (2.5%, 5.0%, 7.5% and 10.0%) nanocomposites. The characteristic peaks of GCN (Fig. 1b) at 13° and 27.5° correspond to the (100) and (002) planes, respectively (JCPDS Card No. 87-1526). The diffraction peaks of GCN at 13° in the SnO_2@GCN nanocomposites were absent. This is due to the very small concentration of GCN present in the nanocomposites. Further, the peak at 27.5° of GCN is overlapped by the SnO_2 peak at 26.6°.[38]

The FTIR spectra of GCN, SnO_2 nanoparticles and SnO_2@GCN (2.5%, 5.0%, 7.5% and 10.0%) nanocomposites are depicted in Fig. 2. In GCN, the peaks at 809 cm^{-1}, 1635 cm^{-1} are because of the out of plane bending modes of heterocyclic C–N, C–N stretching vibration modes and the peaks at (1238, 1317, 1406, 1558) cm^{-1} are due to the aromatic C–N stretching vibration.[39] SnO_2 gives the characteristic Sn–O peaks at 550 cm^{-1} and 640 cm^{-1}. All the samples gave strong absorption peaks around 3150 cm^{-1}, corresponding to the O–H stretching vibration.[40]

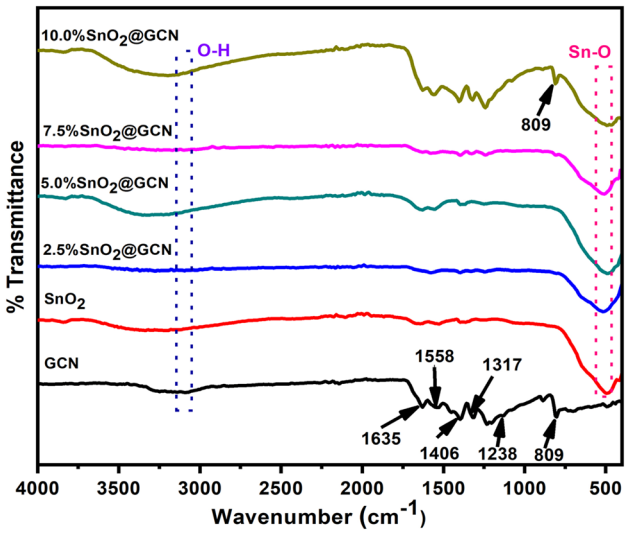

Fig. 2 FTIR spectra of as-synthesized GCN, SnO_2, and various SnO_2@GCN samples.

The characteristics of as-synthesized SnO_2 nanoparticles and SnO_2@GCN nanocomposites (2.5%, 5.0%, 7.5% and 10.0%) and GCN were analysed using Raman spectra. The Raman spectra of SnO_2 nanoparticles and SnO_2@GCN (2.5%, 5.0%, 7.5% and 10.0%) nanocomposites and GCN are shown in Fig. 3. The basic Raman active mode of SnO_2 nanoparticles at 474 cm^{-1} and 621.5 cm^{-1} was observed in the convoluted peak centred at 572 cm^{-1}, whereas another small hump was observed at 768 cm^{-1}. Thus, a Raman spectrum of SnO_2 confirms the formation of rutile SnO_2 nanoparticles. The Raman peaks at 474 cm^{-1}, 621.5 cm^{-1} and 768 cm^{-1} correspond to the E_g, A_{1g} and B_{2g} vibration modes of the rutile SnO_2, which are in

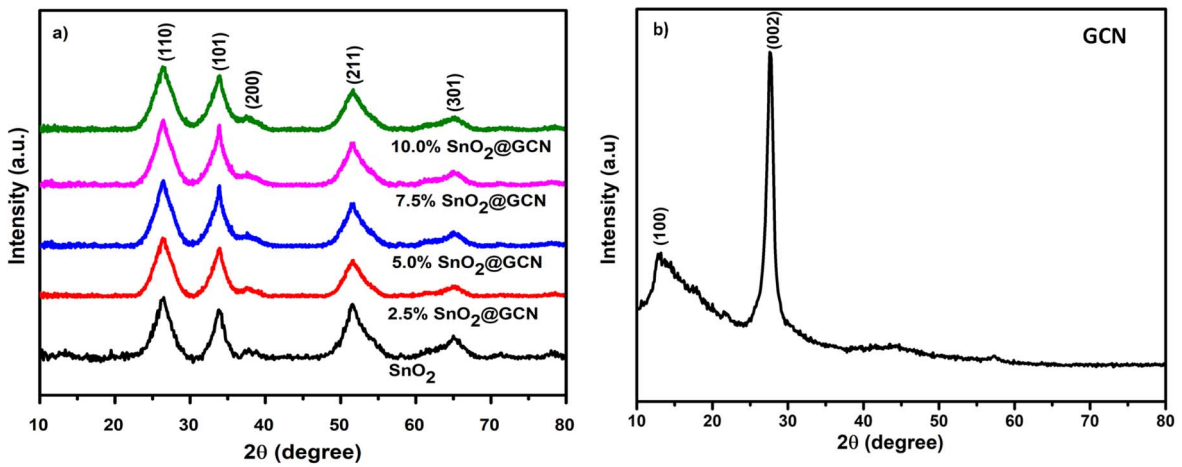

Fig. 1 (a) XRD patterns of as-synthesized SnO_2 and various SnO_2@GCN samples. (b) XRD patterns of as-synthesized GCN.

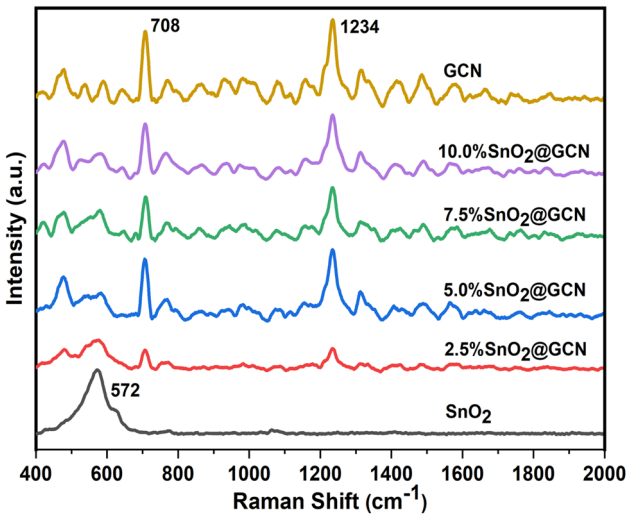

Fig. 3 Raman spectra of SnO_2, GCN and various SnO_2@GCN samples.

accordance with the XRD results.[41] The Raman band at 572 cm^{-1} is attributed to the surface mode of nanostructured SnO_2. The material is crystalline, confirmed by the broadening of Raman peaks. The Raman peak observed at 572 cm^{-1} indicates that the synthesized SnO_2 has a mixed nanocrystalline and amorphous phase. Fig. 3 shows extra vibrational modes located at 708 cm^{-1} and 1234 cm^{-1} in (2.5%, 5.0%, 7.5% and 10.0%) nanocomposites and GCN, but these are not seen in the SnO_2 sample, which means that successful SnO_2@GCN nanocomposites (2.5%, 5.0%, 7.5% and 10.0%) were formed. The intense of vibration modes at 708 cm^{-1}, 1234 cm^{-1} enhances with concentrations of GCN, indicates concentration of GCN increases, which is equivalent to experimental conditions. Additionally, the vibrations at 708 cm^{-1} and 1234 cm^{-1} are assigned to the stretching vibration of aromatic C–N heterocycle characteristic to melem.[42,43] The peaks at 708 cm^{-1} are related to the different types of ring breathing modes of s-triazine.

Thermogravimetric and differential thermal analyses (TGA-DTA) of SnO_2 and 5.0% SnO_2@GCN nanocomposites were recorded up to 700 °C. The TGA-DTA curve of SnO_2 is depicted in Fig. 4a. The TGA curve showed a 11.14% weight loss up to 500 °C due to the loss of water vapour and organic components. After 500 °C, the TGA curve is almost straight. The DTA plot shows two endothermic peaks at 56.30 °C and 274 °C with corresponding weight losses of 4% and 1.6%, respectively. The

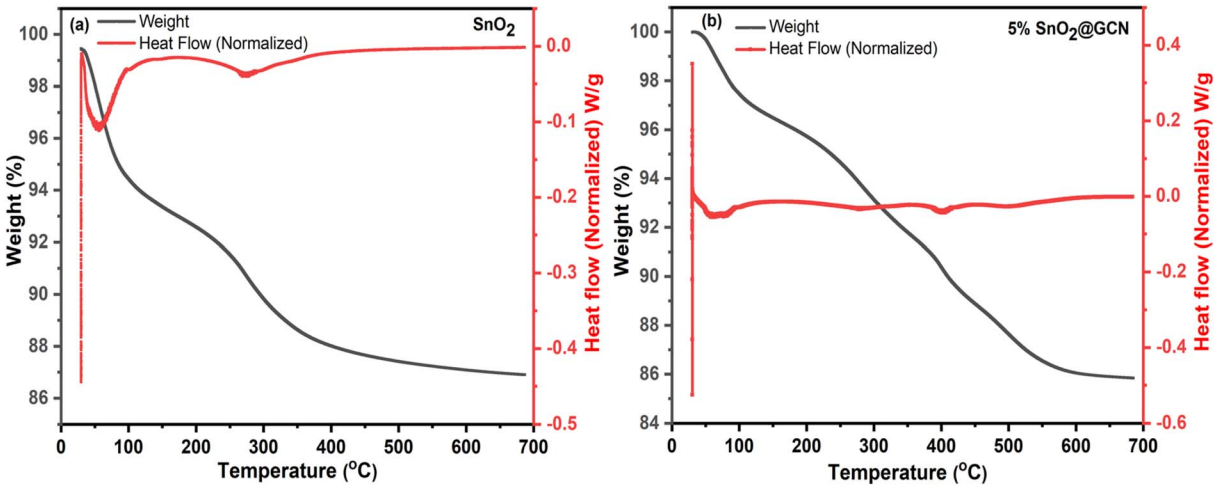

Fig. 4 TGA-DTA curve of (a) SnO_2 and (b) 5% SnO_2@GCN samples.

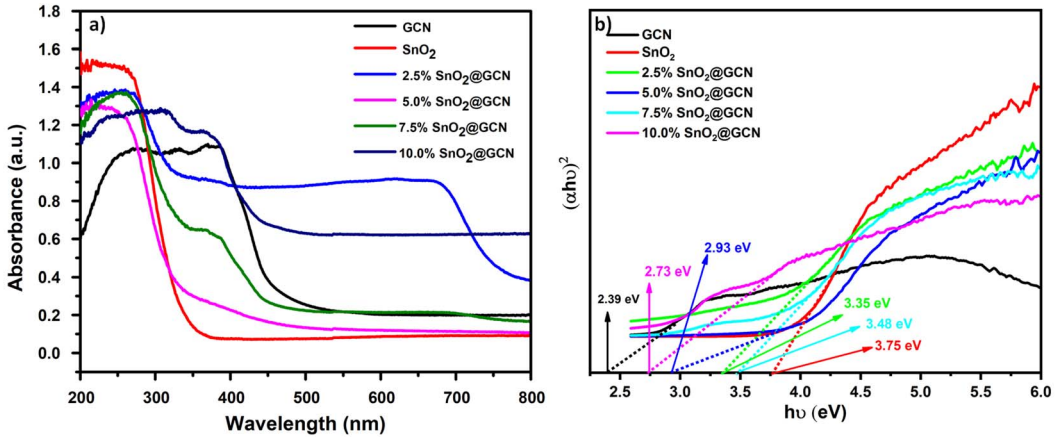

Fig. 5 (a) DRS spectra and (b) UV-vis absorption spectra and band gap determination of GCN, SnO_2, and various SnO_2@GCN samples.

TGA-DTA curve of 5% SnO_2@GCN is depicted in Fig. 4b. The TGA curve shows a 14.55% weight loss up to 600 °C due to the loss of water vapour and organic components. After 600 °C, the TGA curve is almost straight line, it indicates loss of organic compound and formation of stable metal oxide. The DTA plot shows two endothermic peaks at 59 °C and 402 °C with corresponding weight losses of 7.5% and 7.4%, respectively. These results confirm the formation of the 5.0% SnO_2@GCN nanocomposite.

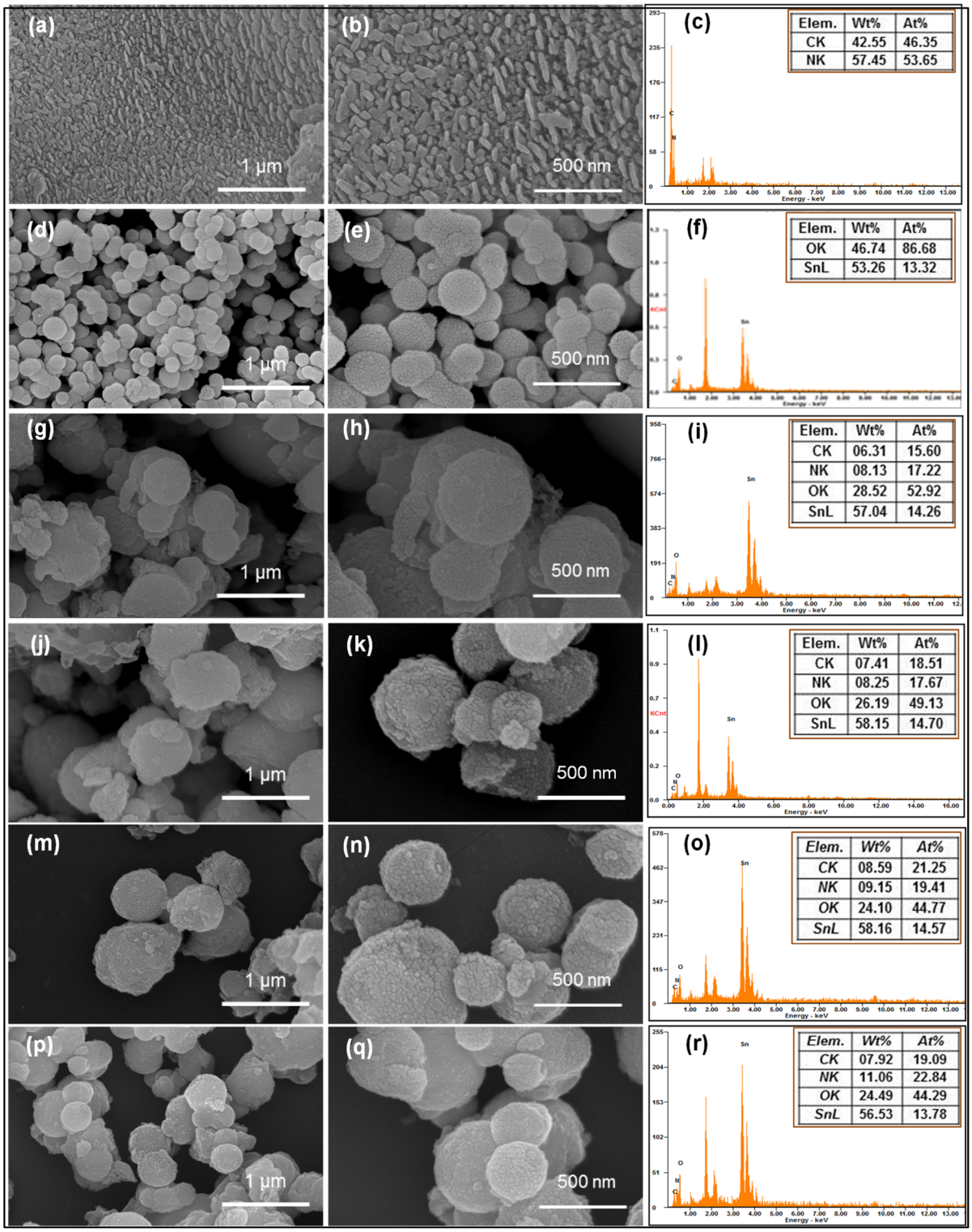

Fig. 6 Low- and high-resolution FESEM images of as-synthesized (a–c) GCN (d–f) SnO_2 (g–i) 2.5% SnO_2@GCN (j–l) 5.0% SnO_2@GCN (m–o) 7.5% SnO_2@GCN and (p–r) 10.0% SnO_2@GCN samples with the corresponding elemental mapping.

The band gap of GCN, SnO_2 nanoparticles and SnO_2@GCN (2.5%, 5.0%, 7.5% and 10.0%) nanocomposites were determined using UV-diffuse reflectance spectroscopy (UV-DRS). The spectra of all the samples were measured in the 200–800 nm wavelength region (Fig. 5a). The band gap of SnO_2 is 3.75, GCN is 2.39 eV, and 5.0% SnO_2@GCN is 2.93 eV. A slight red shift was

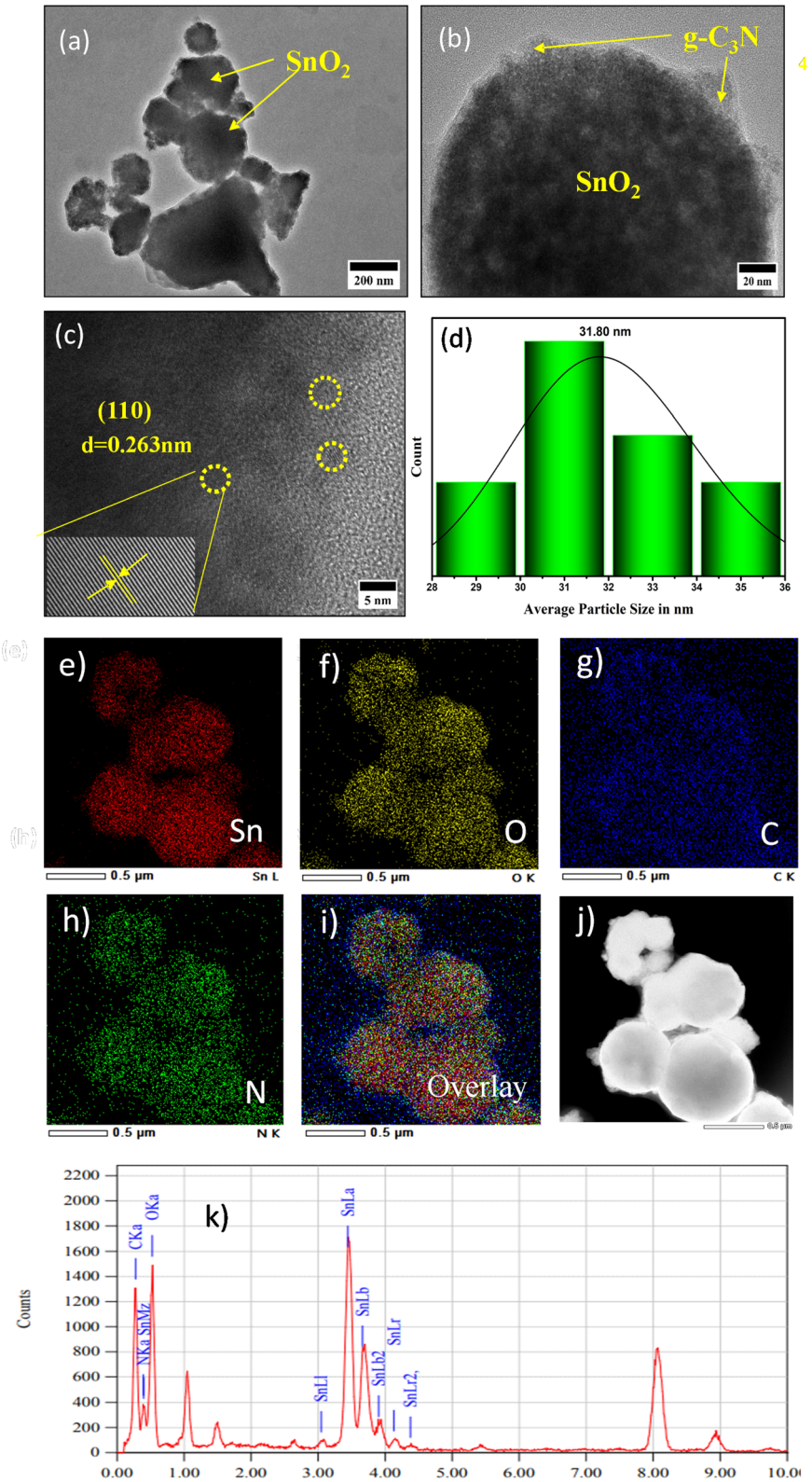

Fig. 7 (a and b) TEM images of the as-synthesized representative 5.0% SnO_2@GCN nanocomposite, (c) HRTEM image, (d) average particle size, (e–j) colour mapping of Sn, O, C and N and (k) EDS elemental mapping of the 5.0% SnO_2@GCN nanocomposite.

observed when SnO_2 is dispersed with g-C_3N_4, which amounts to a decrease in the band gap energy of SnO_2@GCN (2.5%, 5.0%, 7.5% and 10%) nanocomposites as compared with pristine SnO_2 (Fig. 5b). The band gap energy (E_g) was calculated with Tauc's formulae as per the equation given below (1).

$$Ahv = A(hv - E_g)^n \quad (1)$$

E_g is the optical band gap, v is the frequency of light, h is the Planck constant, A is the proportionality coefficient and $n = 2$. It is determined by plotting a graph between $(\alpha hv)^2$ and $hv - (E_g)$.

The morphology of GCN, SnO_2 nanoparticles and SnO_2@GCN (2.5%, 5.0%, 7.5% and 10.0%) nanocomposites at different magnifications were determined with the corresponding elemental mapping (Fig. 6a–r). It is clear from Fig. 6a–r that the

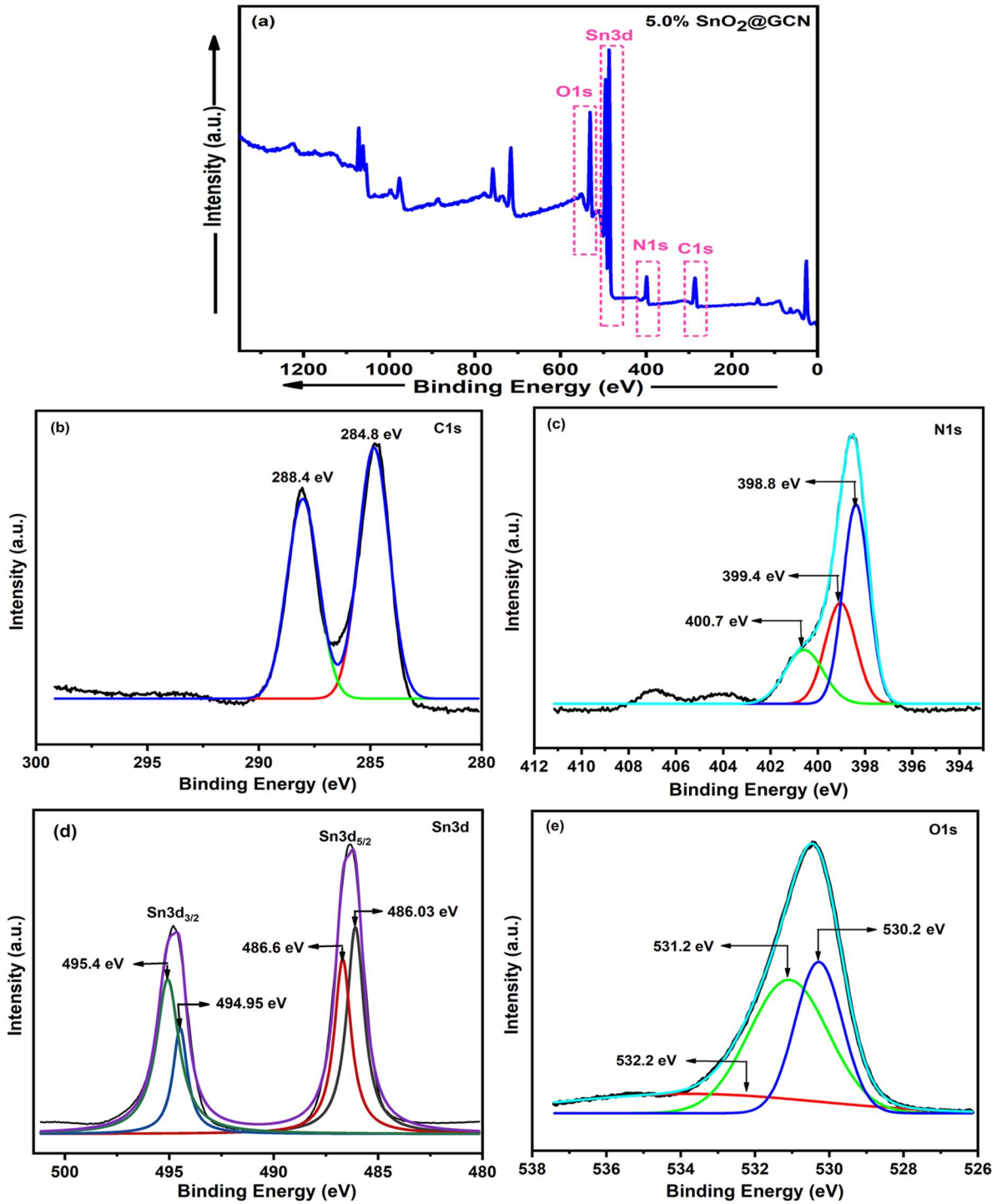

Fig. 8 XPS spectra of the representative 5.0% SnO_2@GCN nanocomposite: (a) survey scans for the 5.0% SnO_2@GCN nanocomposite and (b)–(e) deconvoluted spectrum of C 1s, N 1s, Sn3d, and O 1s.

micrometer scale images are less resolved when compared to nanometer scale images. The FESEM images showed spherical-shaped SnO_2@GCN particles. The particles are agglomerated with a difference in size and porosity. Further, energy dispersive X-ray (EDAX) analysis yielded the elemental compositions within GCN, SnO_2 nanoparticles and SnO_2@GCN (2.5%, 5.0%, 7.5% and 10.0%) nanocomposites. The GCN compound exhibited distinctive peaks corresponding to elements C and N. In contrast, SnO_2 displayed peaks attributed to elements Sn and O. However, 2.5% SnO_2@GCN, 5.0 %SnO_2@GCN, 7.5% SnO_2@GCN and 10.0% SnO_2@GCN showcased peaks indicative of elements Sn, O, C, and N. Notably, the EDAX spectra of the synthesized samples revealed no impurity peaks, confirming the creation of highly pure nanostructures.

The TEM images of the 5.0% SnO_2@GCN nanocomposite (Fig. 7) describe its morphology. The 5.0% SnO_2@GCN nanocomposite exhibits spherical-shaped particles (Fig. 7a and b). TEM images confirm the agglomeration of particles as observed in the FESEM images. The lattice fringes, which determine the crystallographic spacing, are confirmed from the HRTEM image (Fig. 7c). An interplanar distance of 0.263 nm was observed, which is in close agreement with the *d* spacing of the (110)

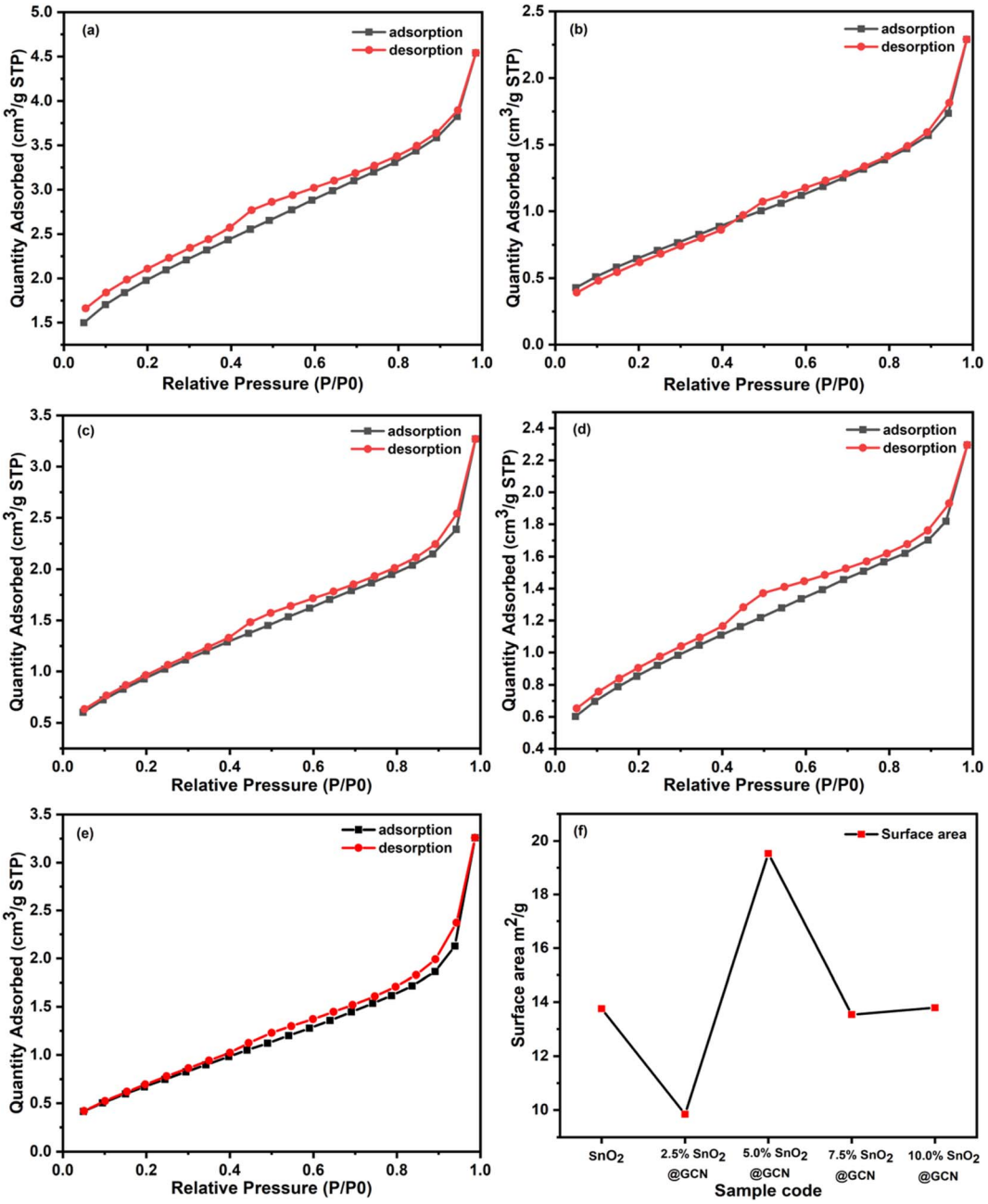

Fig. 9 (a–e) Nitrogen adsorption isotherms of synthesized SnO_2 and various SnO_2@GCN samples (f) plots showing the variation in specific surface area of SnO_2 and various SnO_2@GCN samples.

plane. The average particle size distribution of 5.0% SnO_2@GCN nanocomposite images is given in Fig. 7d. It confirmed the nano-sized crystal material, and the average particle size obtained was 31.80 nm (Fig. 7d, ESI 1†). Individual elements present in the 5.0% SnO_2@GCN nanocomposite, such as Sn, O, C and N, are confirmed by colour mapping (Fig. 7e–j). The elemental composition of the 5.0% SnO_2@GCN nanocomposite (Sn, O, C & N) was confirmed by the energy dispersive spectra (EDS). The synthesized SnO_2@GCN nanocomposites were very pure, as there were no impurity peaks in the spectra (Fig. 7k).

To study the surface properties and oxidation states, XPS spectroscopy was used. The full XPS scan of the 5.0% SnO_2@GCN nanocomposite is depicted in Fig. 8a. In the survey scan of metals, C 1s, N 1s, O 1s and Sn3d main photoionization signals were obtained. To investigate the oxidation states, relative intensities of the narrow scan for long-time measured patterns of C 1s, N 1s, Sn3d and O 1s bands were studied and are shown in Fig. 8b–e, respectively. The 5.0% SnO_2@GCN nanocomposite has binding energy peaks at 284.8 eV and 288.4 eV, which correspond to C 1s. The peaks at 398.8 eV, 399.4 eV and 400.7 eV for N 1s correspond to the sp2 nitrogen present in triazine rings (C–N=C), tertiary nitrogen groups and free amino groups (C–N–H), respectively. The core signals of other metal ions, such as signals for O 1s, were at 530.2 eV, 531.2 eV and 532.2 eV. For Sn $3d_{5/2}$, the peaks are at 486.03 eV and 486.6 eV; for Sn $3d_{3/2}$, the peaks were at 494.95 eV and 495.4 eV. These observations support the formation of the 5.0% SnO_2@GCN nanocomposite.

The N_2 adsorption/desorption isotherms of SnO_2, 2.5% SnO_2@GCN, 5.0% SnO_2@GCN, 7.5% SnO_2@GCN and 10.0% SnO_2@GCN nanocomposites are depicted in Fig. 9a–e respectively. To examine the surface area, Brunauer, Emmett, and Teller (BET) surface area measurements were carried out in liquid nitrogen at 77.35 K. Further, the Barrett–Joyner–Halenda (BJH) pore size distribution of all synthesized compounds, SnO_2, 2.5% SnO2@GCN, 5.0% SnO2@GCN, 7.5% SnO2@GCN and 10.0% SnO2@GCN nanocomposites, were investigated. The surface area and morphological properties play a very important role in photocatalyst application, which could increase the contact interaction between the catalyst and the dye, enhancing the photocatalytic activity. The estimated values of specific surface area, average pore radius and total pore volume were determined (Table 1). The maximum specific surface area was observed for the 5.0% SnO_2@GCN nanocomposite (Fig. 9f). The 5.0% SnO_2@GCN nanocomposite with a high specific surface area showed good photocatalytic activity as compared to SnO_2, 2.5% SnO_2@GCN, 7.5% SnO_2@GCN and 10.0% SnO_2@GCN nanocomposites. Fig. 10 represents the BJH pore size distribution of all five samples of SnO_2, 2.5% SnO_2@GCN, 5.0% SnO_2@GCN, 7.5% SnO_2@GCN and 10.0% SnO_2@GCN

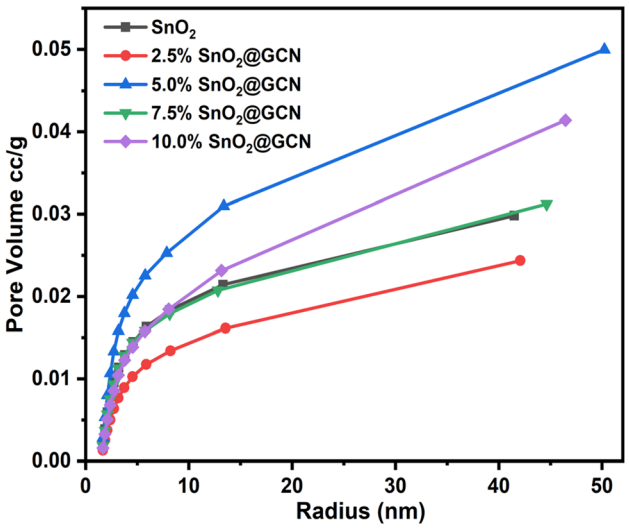

Fig. 10 BJH pore size distribution of SnO_2 and various SnO_2@GCN nanocomposites.

nanocomposites. The 5.0% SnO_2@GCN nanocomposite exhibits a high specific surface area and pore volume (Table 1), which results in providing maximum sites for the reaction, adsorption as well as desorption and exposure of the inner surface of the material, and it is beneficial in photocatalyst application. The investigation focused on the photodegradation of MB dye in solar light over SnO_2@GCN composites. The efficiency of decolorization was evaluated, and the photocatalytic process was monitored by utilizing the 663 nm optical absorption peak. The photodegradation of aqueous MB dye using SnO_2@GCN composites is illustrated (Fig. 11a–e). It is evident that, in all cases, the absorbance of the MB dye gradually decreased with respect to the respective catalysts and irradiation time without any observable shifts in the spectrum. Notably, 5.0% SnO_2@GCN exhibited more degradation compared to other photocatalysts. Additionally, we conducted a recyclability test for the 5.0% SnO2@GCN composite, as illustrated in Fig. 11f, and the results demonstrate that the sample exhibits good recyclability after five consecutive cycles, confirming its stability.

In Fig. 12a, the photodegradation plot of MB dye using different photocatalysts in solar light as a function of time is presented. A controlled experiment (no catalyst) was performed, revealing that the dye solution remained unchanged after irradiation under solar light. The photodegradation rate was observed to be higher for 5.0%SnO_2@GCN compared to other samples. 5.0% SnO_2@GCN demonstrated the highest photocatalytic activity, reaching almost 97%. The observed MB dye

Table 1 Specific surface area and pore parameters

Surface area and pore parameters	SnO_2	2.5%SnO_2 @GCN	5.0%SnO_2 @GCN	7.5%SnO_2 @GCN	10.0%SnO_2 @GCN
Specific surface area ($m^2\ g^{-1}$)	13.7544	9.8458	19.5299	13.5362	13.7901
Total pore volume ($cm^3\ g^{-1}$)	0.0298	0.0243	0.0499	0.0312	0.0414
Average pore radius (nm)	1.6874	1.6788	1.6869	1.6889	1.6859

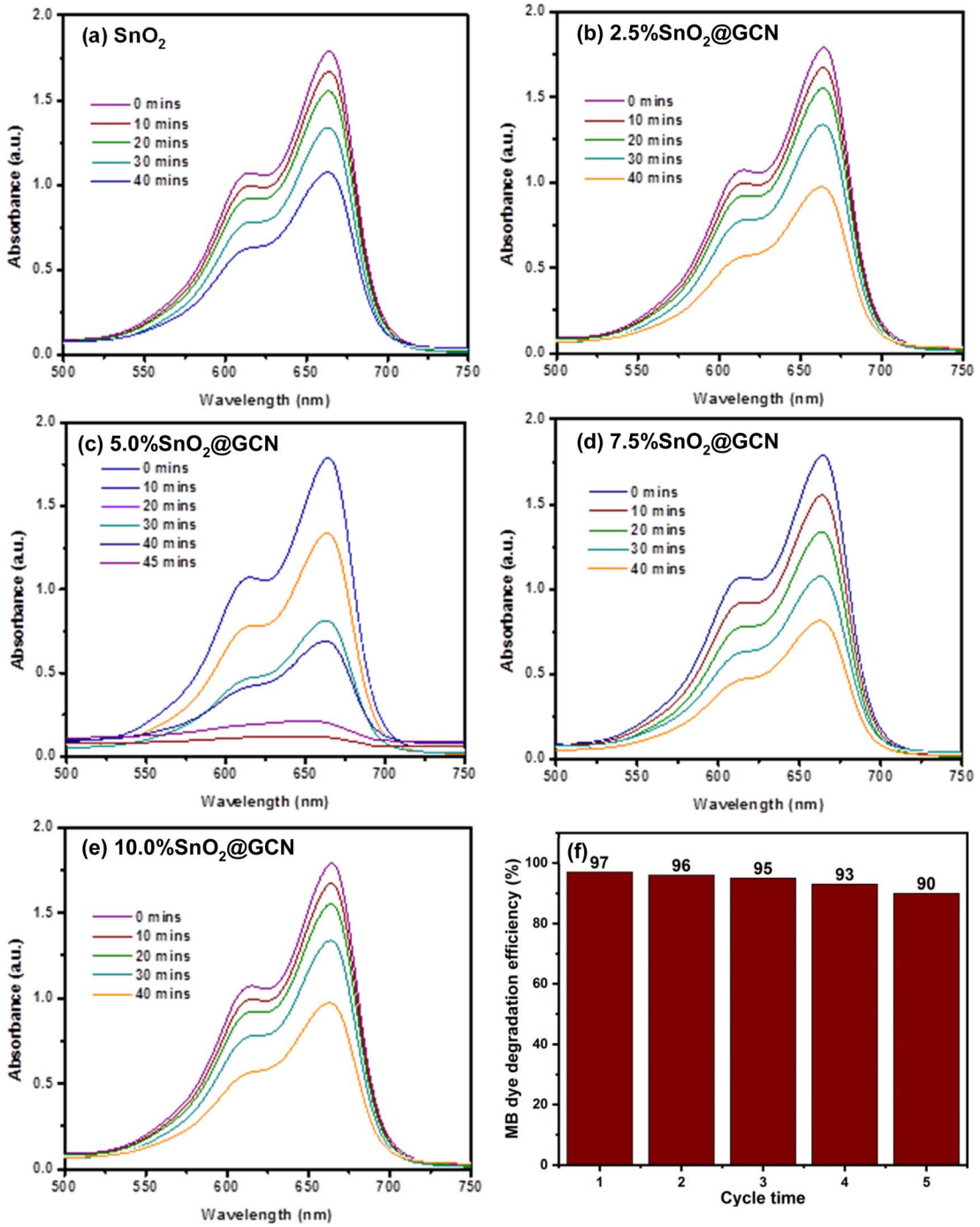

Fig. 11 (a–e) Time-dependent changes in the absorption spectra of the MB dye aqueous solution (100 ppm, 100 ml) in the presence of 10 mg of SnO_2 and various SnO_2@GCN samples under sunlight irradiation, along with the corresponding colour changes in the initial solution at 10–45 minutes of the photodegradation reaction. (f) Recyclability of the 5% SnO_2@GCN nanocomposite.

photodegradation rate followed the order: 5.0% SnO_2@GCN > 7.5% SnO_2@GCN > 2.5% SnO_2@GCN > SnO_2 > 10.0% SnO_2@GCN. Thus, we can conclude that with an increase in the loading of GCN up to 5 wt%, degradation increases; however, after that, the rate of degradation decreases for 7.5% and 10.0% (SnO_2@GCN) samples.

Fig. 12b displays the plot of ln (C_t/C_0) *versus* irradiation time of MB degradation in the presence of photocatalysts. The rate constants were estimated for SnO_2 nanoparticles, 2.5% SnO_2@GCN, 5.0% SnO_2@GCN, 7.5% SnO_2@GCN and 10.0% SnO_2@GCN nanocomposites, yielding values of 0.0125, 0.0382, 0.0902, 0.0589, and 0.0456, respectively (see Table 2). Notably, in contrast to previous investigations, the MB degradation for the 5.0% SnO_2@GCN sample is significantly higher.[44–47] The higher photodegradation is attributed to the band structure,

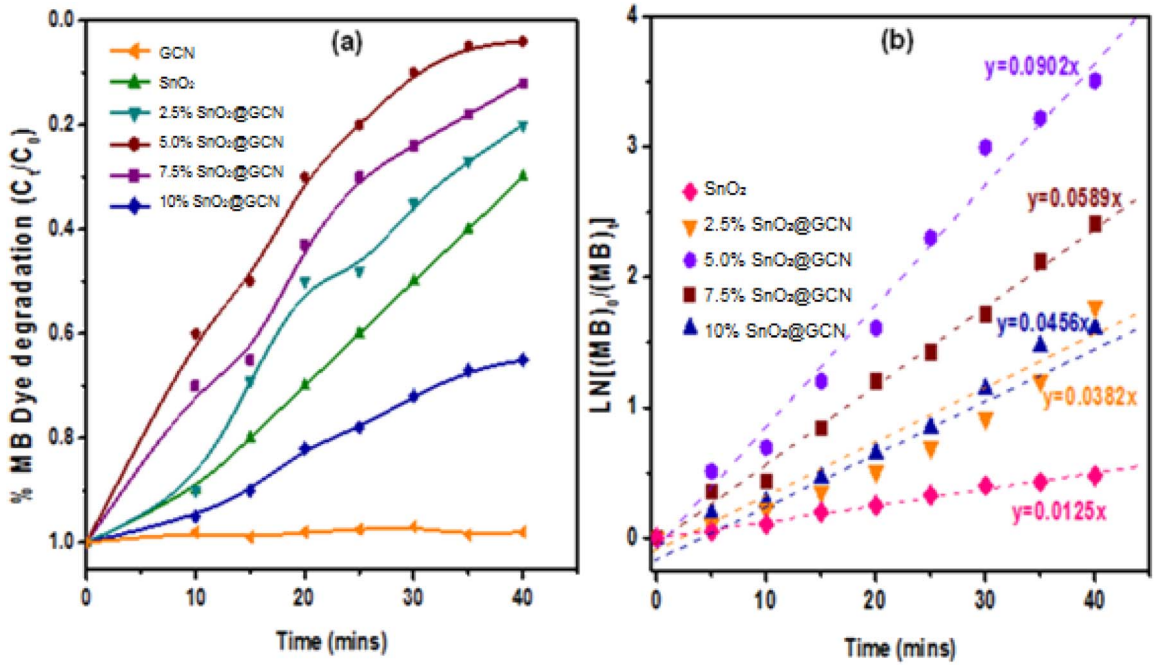

Fig. 12 (a) Plot of the MB-normalized concentration with GCN, SnO_2 and various SnO_2@GCN catalysts with solar radiation as a function of time. (Initial concentration: 100 ppm, 100 ml; each catalyst conc. 10 mg). (b) Plot of ln (C_t/C_0) *versus* irradiation time of MB degradation in the presence of as-synthesized catalysts.

Table 2 Kinetic parameters for as-synthesized samples

Sample	Rate equation	Correlation coefficient R^2
SnO_2	$y = 0.0125x$	$R^2 = 0.9702$
2.5% SnO_2@GCN	$y = 0.0382x$	$R^2 = 0.9842$
5.0% SnO_2@GCN	$y = 0.0902x$	$R^2 = 0.9923$
7.5% SnO_2@GCN	$y = 0.0589x$	$R^2 = 0.9914$
10.0% SnO_2@GCN	$y = 0.0456x$	$R^2 = 0.9716$

morphology, interface, and high crystallinity of 5.0%SnO_2@g-C_3N_4, resulting in maximum MB degradation.

After conducting the MB dye degradation using SnO_2@g-C_3N_4, we extended our investigation to the degradation of a colourless contaminant, BPA. This was particularly relevant given that MB is photosensitive under solar light. We examined the photocatalytic efficiency of the as-synthesized SnO_2 and SnO_2@GCN catalysts for the photodegradation of BPA. The degradation performance of different SnO_2 and SnO_2@GCN photocatalysts is illustrated in Fig. 13a. The results indicate that SnO_2@GCN photocatalysts exhibit superior photocatalytic efficiency, with the 5.0% SnO_2@GCN composite demonstrating the highest photoactivity, degrading approximately 99% of BPA within 60 minutes under solar light irradiation.

Further, Fig. 13b shows the effect of different dosages of 5.0% SnO_2@GCN on BPA degradation. The catalyst dosages were varied between 0.25 g L^{-1} and 1.0 g L^{-1}. It was observed that the degradation efficiency increased with the catalyst dosage, reaching an optimum at 0.75 g L^{-1}. Beyond this dosage, at 1.0 g L^{-1}, the degradation efficiency declined. This phenomenon can be attributed to the well-known fact that increasing the photocatalyst dosage generates more reactive species (*e.g.*, radicals), which enhances photoactivity. However, exceeding the optimal dosage can lead to increased suspension opacity, inhibiting light penetration and promoting agglomeration, which reduces the active surface area available for photocatalysis, thus lowering the degradation efficiency.

Additionally, Fig. 13c illustrates the effect of varying the initial concentration of BPA on the photodegradation efficiency. The results reveal that as the initial BPA concentration increased, the degradation efficiency decreased. This can be explained by the limited number of active sites on the 1 g L^{-1} 5.0% SnO_2@GCN catalyst, which are insufficient to degrade higher concentrations of BPA, such as 45 mg L^{-1}, leading to reduced photoactivity.

The influence of the initial pH on BPA degradation was also studied by adjusting the pH with HCl and NaOH, and the results are presented in Fig. 13d and e. The data show that the minimum degradation (~82%) occurred at pH 10, while the degradation efficiency increased as the pH approached neutral (pH 6). This can be attributed to the interaction between BPA degradation efficiency and the ionic environment, as well as the surface charge of the SnO_2@GCN photocatalyst. At pH < 6, the presence of Cl^- ions may compete with BPA for adsorption on the catalyst surface, thereby reducing the degradation efficiency.

Fig. 13f further explores the effect of different cations and anions on BPA degradation. The results indicate that the addition of cations such as K^+, Na^+, and Ca^{2+} led to a slight increase in degradation efficiency, likely due to the reduction in

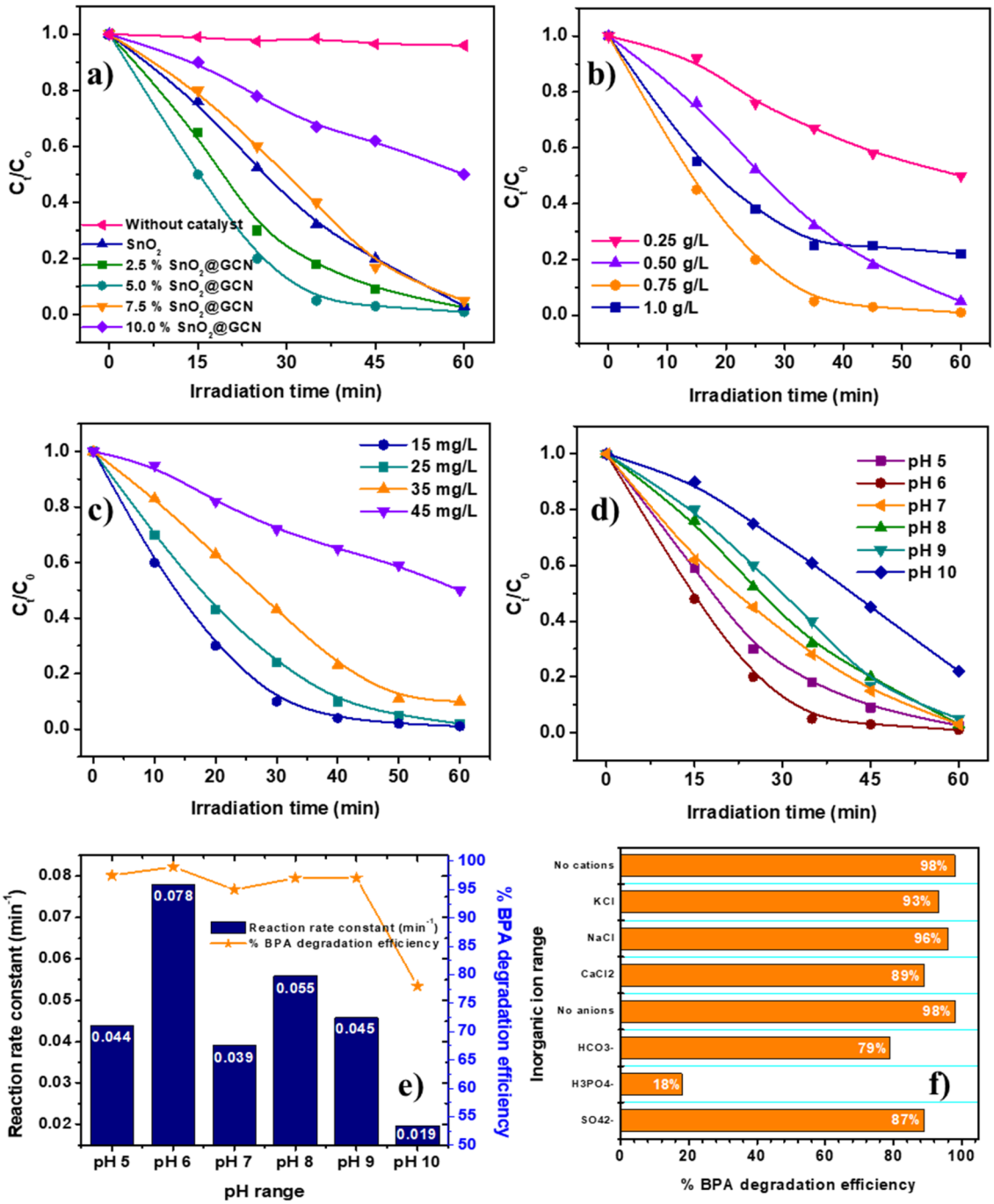

Fig. 13 (a) Effect of different as-synthesized pristine SnO_2 and SnO_2@GCN photocatalysts on BPA degradation. (b) Effect of 5% SnO_2@GCN photocatalyst dosage on BPA degradation. (c) Effect of initial BPA concentration on photodegradation (5% SnO_2@GCN dosage = 1.0 g L^{-1} and pH = 6.5). (d) Effect of pH on BPA photodegradation (Initial BPA concentration = 35 mg L^{-1} and 5% SnO_2@GCN dosage = 1.0 g L^{-1}). (e) Effect of pH on the reaction rate constant over 5% SnO_2@GCN photocatalyst under sunlight irradiation (Initial BPA concentration = 35 mg L^{-1} and 5% SnO_2@GCN dosage = 1.0 g L^{-1}). (f) Effect of inorganic ions on % BPA photodegradation.

the thickness of the electric double layer surrounding the photocatalyst particles. On the contrary, the addition of anions such as HCO_3^-, $H_3PO_4^{\bullet-}$, and SO_4^{2-} had a detrimental effect on the degradation process, with the minimum degradation (~18%) observed in the presence of H_3PO_4. This reduction in degradation efficiency can be explained by the role of anions as scavengers of hydroxyl radicals and photogenerated holes, which are essential for the photocatalytic degradation of BPA.

The 5.0% SnO_2@GCN composite exhibited superior photocatalytic activity for BPA degradation under optimal conditions. However, the catalyst dosage and environmental factors, such as pH and the presence of competing ions, significantly influenced the degradation efficiency. These findings underscore the

importance of optimizing the reaction conditions to maximize the photocatalytic performance of SnO_2@GCN composites for the degradation of organic pollutants such as BPA.

Electrochemical impedance spectroscopy (EIS) and photocurrent measurements are crucial parameters for evaluating the separation efficiency of photoinduced charge carriers in photocatalysis. EIS was utilized to further assess the separation efficiency of electron–hole pairs (Fig. 14a). The semicircle radius of the Nyquist plots provides insights into the charge carrier transfer rate; a smaller semicircle radius indicates lower resistance, and therefore, more efficient charge transfer.[48] The 5.0% SnO_2@GCN composite displays a smaller semicircle radius than pure SnO_2 and the other composites, underscoring its superior charge separation and transfer efficiency. The enhanced charge transfer resistance is attributed to the loading of GCN in the nanocomposites (Fig. 14a).[49,50]

The photocurrent response of both pristine graphitic carbon nitride (GCN) and the 5.0% SnO_2@GCN composite was investigated, as illustrated in Fig. 14b. The results clearly demonstrate that the 5% SnO_2@GCN composite generates a significantly higher photocurrent than the pure GCN. This enhanced photocurrent response indicates a more efficient separation and transportation of photogenerated charge carriers in the composite material. The improved charge carrier dynamics can be attributed to the synergistic interaction between SnO_2 and GCN, which effectively suppresses the recombination of photoinduced electron–hole pairs. Such behaviour suggests that the incorporation of SnO_2 nanoparticles into the GCN matrix enhances its photoelectrochemical performance, making it a promising candidate for application in photocatalysis.[9,10]

Furthermore, the stability of the 5.0% SnO_2@GCN composite was evaluated through FESEM and FTIR analyses conducted before and after the photocatalytic experiments, as presented in Fig. ESI 2 and 3.† The comparative analysis revealed no significant morphological or structural changes, indicating that the 5.0% SnO_2@GCN composite maintains good stability during the photocatalytic process.

These results collectively demonstrate that incorporating 5.0% GCN into SnO_2 significantly enhances photocatalytic performance by improving the charge carrier separation and reducing recombination rates. This enhancement is likely due to the synergistic effects between GCN and SnO_2, facilitating better charge transport and extending the lifespan of charge carriers. Consequently, the 5.0% SnO_2@GCN composite stands out as a promising candidate for advanced photocatalytic applications.

The role of active radicals in degrading the MB dye using the 5.0% SnO_2@GCN photocatalyst was studied *via* radical trapping.[51] To capture holes, hydroxyl radicals, and superoxide radicals, 1 mmol of ethylenediaminetetraacetic acid (EDTA), isopropanol (IPA), and benzoquinone (BQ) were added to the system. Fig. 15a shows that the photocatalytic activity of 5.0% SnO_2@GCN photocatalyst decreases significantly with IPA and BQ, indicating that $^{\bullet}OH$ and $O_2^{\bullet-}$ are the main oxidative species.[52] The activity remains unchanged with EDTA, proving that holes are not the primary active species.

These results highlight that the degradation rate of MB dye depends on the hydroxyl and superoxide radicals. The 5.0% SnO_2@GCN incorporation enhances the generation of these radicals by improving the charge separation and increasing surface area, leading to better interaction with the dye molecules. This improved activity suggests that the SnO_2@GCN composites are promising for environmental remediation, where efficient organic pollutant degradation is crucial.

The remarkable photocatalytic activity exhibited by the 5.0% SnO_2@GCN nanocomposite suggests an efficient mechanism for the solar-driven degradation of methylene blue (MB). As depicted in Fig. 15b, the degradation process is likely governed by a direct Z-scheme charge transfer mechanism, as supported by recent literature.[53–55] In this system, the band structure of the composite plays a critical role in facilitating efficient charge separation and enhancing photocatalytic efficiency. The positions of the conduction band (CB) and valence band (VB) edges were theoretically estimated using eqn (2) and (3):[56]

$$E_{CB} = \chi - E_e - 0.5\,E_g \quad (2)$$

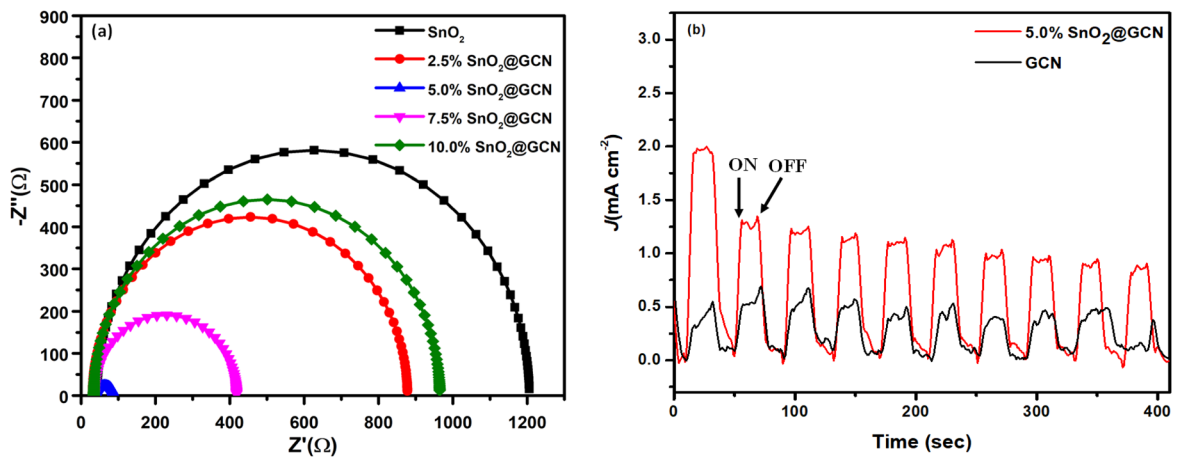

Fig. 14 (a) Electrochemical impedance spectra (EIS) of SnO_2, 2.5% SnO_2@GCN, 5.0% SnO_2@GCN, 7.5% SnO_2@GCN, and 10.0% SnO_2@GCN composites. (b) Photocurrent response spectra of GCN and 5.0% SnO_2@GCN composite.

$$E_{VB} = E_{CB} + E_g \quad (3)$$

Here, E_{CB} and E_{VB} represent the potential at the conduction band and valence band edges, respectively; E_e is the free electron energy (approximately 4.5 eV) in the hydrogen spectrum; Eg is the semiconductor band gap energy; and χ is the absolute electronegativity of the semiconductor. Based on these calculations, SnO_2 exhibits VB and CB potentials of +3.65 eV and +0.05 eV, respectively, while g-C_3N_4 shows the VB and CB positions of +1.42 eV and −0.96 eV, respectively. Under solar illumination, both SnO_2 and g-C_3N_4 are excited to generate electron–hole pairs. In the Z-scheme configuration, electrons from the CB of SnO_2 recombine with holes from the VB of g-C_3N_4, leaving highly active electrons in the CB of g-C_3N_4 and holes in the VB of SnO_2. The strong oxidizing holes (+3.65 eV) in the VB of SnO_2 readily oxidize H_2O molecules to generate hydroxyl radicals ($^{\bullet}OH$), which are powerful oxidants for dye degradation. Simultaneously, the electrons accumulated in the CB of g-C_3N_4 (at −0.96 eV) reduce O_2 to produce superoxide radicals ($O_2^{\bullet-}$). These reactive oxygen species work synergistically to achieve efficient MB degradation.[57]

This direct Z-scheme mechanism not only improves the spatial separation of photogenerated charges but also preserves their strong redox capabilities, thereby enhancing photocatalytic performance. The proposed mechanism aligns well with recent findings reported for similar SnO_2-based Z-scheme photocatalysts,[58] further validating our approach. Additionally, supporting evidence from scavenger experiments, photoluminescence quenching, and active species trapping studies in recent reports corroborate the Z-scheme pathway in similar composite systems.[59,60]

The SnO_2@GCN nanocomposite materials applied in photocatalysis, as reported in the literature, are summarized (Table 3). We can conclude from Table 3 that the SnO_2@GCN nanocomposite photocatalysts synthesized by the hydrothermal

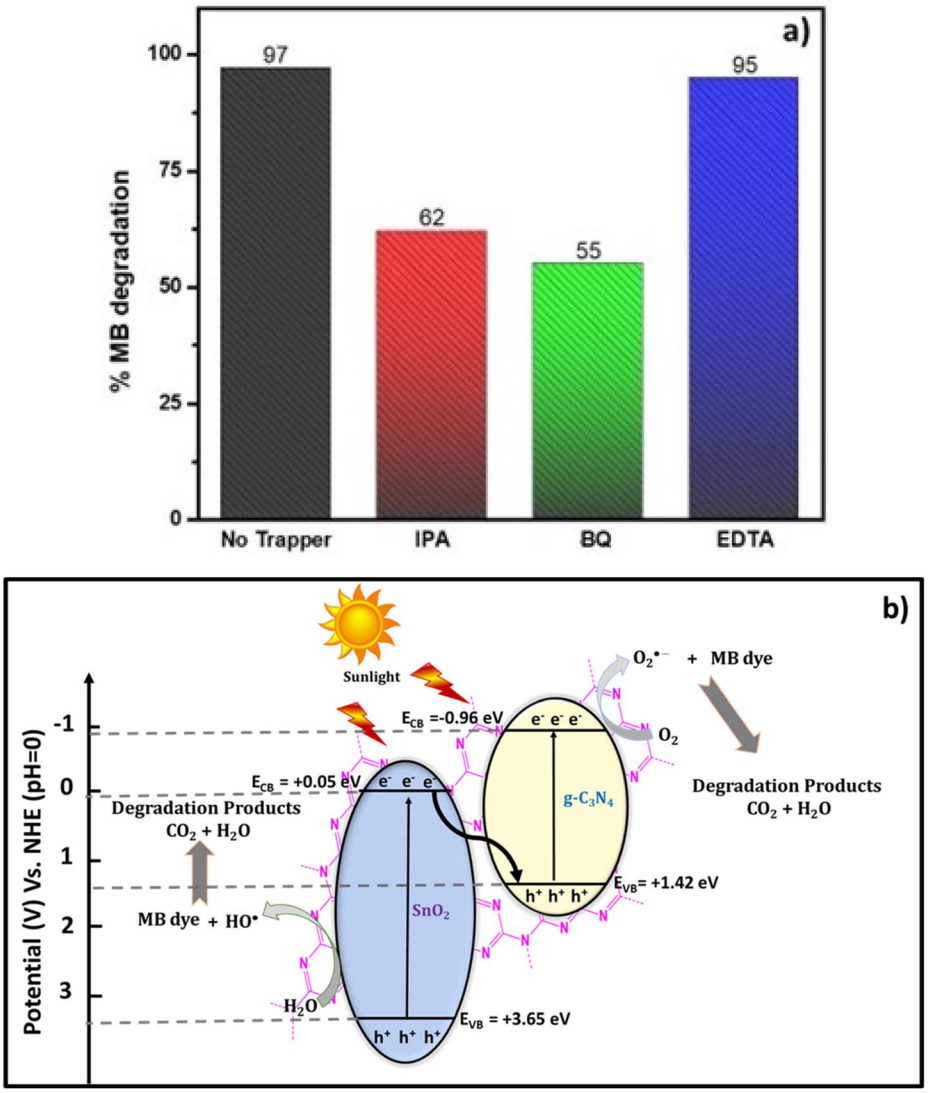

Fig. 15 (a) Influence of different scavengers on the photodegradation efficiency of methylene blue using 5% SnO_2@GCN and (b) photodegradation mechanism of MB dye using the SnO_2/g-C_3N_4 (5.0% SnO_2@GCN) nanocomposite.

Table 3 Summary of the recent research reports pertaining to the synthesis of SnO_2@g-C_3N_4 nanocomposites and their application as photocatalysts

Photocatalyst	Method	Dye soln. tested	Light source	Remark	References
SnO_2@g-C_3N_4	Hydrothermal	MB 10 mg L^{-1}	Visible light	99.38% 75 min	61
50% SnO_2@g-C_3N_4	Hydrothermal	RhB 10 mg L^{-1}	Visible light	99.38% 120 min	62
SnO2@g-C3N4 40%	Hydrothermal	RhB 10 mg L^{-1}	UV light	100% 240 min	63
			Visible light	98.5% 240 min	
SnO_2@g-C_3N_4	Hydrothermal	Methyl orange 1×10^{-5} mol L^{-1}	Visible light	120 min	64
QDs SnO_2@g-C_3N_4	Co-precipitation	Methyl orange 5 mg L^{-1}	Sunlight	94% 180 min	65
16.5% SnO_2@g-C_3N_4	Hydrothermal	Methyl orange	Visible light	58% 180 min	66
SnO_2@g-C_3N_4	Sol–gel	Methyl orange 2×10^{-5} M	Visible light	83% in 150 min	67
SnO_2@g-C_3N_4	Hydrothermal	MB 10 mg L^{-1}	Sunlight	97% 45 min	Present work

method are superior to other materials due to their higher competing photocatalytic activity[61–67] compared to other photocatalysts.

4. Conclusion

In conclusion, the SnO_2@g-C_3N_4 nanocomposites were successfully synthesized and characterized, revealing significant insights into their structural, morphological, and photocatalytic properties. XRD confirmed the formation of tetragonal rutile SnO_2 and g-C_3N_4, with observed band gap modifications. SEM and TEM revealed spherical morphology and uniform nano-sized particles, while EDAX and XPS confirmed the elemental composition and purity. BET analysis indicated an enhanced specific surface area for the 5.0% SnO_2@GCN composite, correlating with its superior photocatalytic performance. The SnO_2@GCN heterojunctions achieved 97% photocatalytic degradation efficiency for methylene blue (MB) under sunlight in 45 minutes, surpassing pure SnO_2 and g-C_3N_4. Additionally, the SnO_2@GCN composites demonstrated 99% degradation efficiency for BPA within 60 minutes under sunlight, further highlighting their potential for environmental remediation. This performance enhancement is due to improved charge separation and extended sunlight absorption from the SnO_2 and g-C_3N_4 synergy. The Z-scheme charge transfer mechanism further clarified the charge dynamics within the composite, solidifying the SnO_2@GCN nanocomposite as a promising candidate for efficient solar-driven photocatalysis in wastewater treatment.

Data availability

The data will be made available on request.

Author contributions

Vaibhav Salve: format analysis, methodology, investigation, catalyst preparation, photodegradation studies, and kinetic studies. Pramod Agale: format analysis, methodology, investigation, and catalyst preparation. Sagar Balgude: plotting of the graphs and synthesis of material. Satish Mardikar: plotting, software run, and photodegradation studies. Sonaba Dhotre: format analysis, methodology, and investigation. Paresh More: conceptualization of idea, writing review and editing, writing original manuscript and supervision.

Conflicts of interest

There are no conflicts to declare.

Acknowledgements

V. S, P. A and P. M are thankful to the Management, Secretary Dr B. B. Sharma, Principal Prof. Preeta Nilesh of K. E. T'S, V. G. Vaze College Autonomous, for extending laboratory facilities, encouragement and support.

References

1 M. Najjar, H. Ali Hosseini, A. Masoudi, Z. Sabouri, A. Mostafapour, M. Khatami and M. Darroudi, Green chemical approach for the synthesis of SnO_2 nanoparticles and its application in photocatalytic degradation of Eriochrome Black T dye, *Optik*, 2021, **242**, 167152, DOI: 10.1016/j.ijleo.2021.167152.

2 Z. Li, J. Zhang, R. Wu, P. Qiu, Y. Yao, X. Liao, Y. Jiang, J. Shi, Y. Chen and S. Lu, An S-scheme α-Fe_2O_3/g-C_3N_4 heterojunction nanostructure with superior visible-light photocatalytic activity for the aza-Henry reaction, *J. Mater. Chem. C*, 2022, **45**, 17075–17083, DOI: 10.1039/D2TC03866H.

3 A. Verma, E. Dhanaraman, W.-T. Chen and Y.-P. Fu, Optimization of Intercalated 2D BiOCl Sheets into Bi_2WO_6 Flowers for Photocatalytic NH_3 Production and Antibiotic Pollutant Degradation, *ACS Appl. Mater. Interfaces*, 2023, **15**, 37540–37553, DOI: 10.1021/acsami.3c07489.

4 A. P. Singh, S. Kumar and M. Thirumal, Efficient Charge Transfer in Heterostructures of CdS/$NaTaO_3$ with Improved Visible-Light-Driven Photocatalytic Activity, *ACS Omega*, 2019, **4**, 12175–12185, DOI: 10.1021/acsomega.9b01133.

5 K. Jangam, S. Balgude, H. Pawar, S. Patange and P. More, Effect of cobalt substitution in Zn1-xCoxFeCrO4 ferrichromate: emerging light absorber for degradation of model textile dye, *Surf. Interfaces*, 2022, **33**, 102189, DOI: 10.1016/j.surfin.2022.102189.

6 S. Balgude, K. Patil, S. Moharil, M. Puranik, S. Kadam, P. Lokhande, S. Patange and P. More, Magnetically

Separable $Zn_{1-x}Cu_{0.5x}Mg_{0.5x}Fe_2O_4$ Ferrite: A Stable Catalyst for Reduction of 4-Nitrophenol, *ChemistrySelect*, 2022, **7**, e202200221, DOI: 10.1002/slct.202200221.

7 P. Agale, V. Salve, S. Mardikar, S. Patange and P. More, Synthesis and characterization of hierarchical Sr-doped ZnO hexagonal nano disks as an efficient photocatalyst for the degradation of methylene blue dye under sunlight irradiation, *Appl. Surf. Sci.*, 2024, **672**, 160795, DOI: 10.1016/j.apsusc.2024.160795.

8 P. More, K. Jangam, S. Kadam, S. Balgude, S. Ajagekar and R. Yamgar, Co3O4 supported on MWCNT: A highly efficient nano composite for the adsorption of Coracryl yellow dye and in the reduction of 4-Nitrophenol, *Results Chem.*, 2023, **5**, 100963, DOI: 10.1016/j.rechem.2023.100963.

9 Y. Zhu, D. Zhu, Q. Yan, G. Gao, J. Xu, Y. Liu, S. Alahakoon, M. Rahman, P. Ajayan, E. Egap and R. Verduzco, Metal Oxide Catalysts for the Synthesis of Covalent Organic Frameworks and One-Step Preparation of Covalent Organic Framework-Based Composites, *Chem. Mater.*, 2021, **33**, 6158–6165, DOI: 10.1021/acs.chemmater.1c01747.

10 Y. Z. Liu, Q. Ai, G. Gao, L. Yuan, Q. Fang, X. Tian, X. Zhang, E. Egap, P. Ajayan and J. Lou, In Situ Synthesis of Lead-Free Halide Perovskite-COF Nanocomposites as Photocatalysts for Photoinduced Polymerization in Both Organic and Aqueous Phases, *ACS Mater. Lett.*, 2022, **4**, 464–471, DOI: 10.1021/acsmaterialslett.1c00785.

11 H. Yang, X. Yan, C. Yan, Z. Min, L. Chai, C. Wang, L. Chen, W. Xiao, T. Wang, C. Xie, D. Pang and X. Fei Li, Revealing interaction of pyridinic N in N-doped carbon with Sn sites for improved CO_2 reduction, *Rare Met.*, 2024, **43**(11), 6096–6104, DOI: 10.1007/s12598-024-02795-6.

12 H. Li, K. Yu, X. Jing, L. Duan and Y. Zhang, Design and preparation of highly crystalline K-intercalated W@PCN: an efficient material for aniline elimination, *Rare Met.*, 2024, **43**(3), 1337–1342, DOI: 10.1007/s12598-023-02473-z.

13 S. Ramasundaram, V. Manikandan, P. Vijayalakshmi, S. Devanesan, M. Salah, A. C. Ramesh Babu, A. Priyadharsan, T. Hwan Oh and S. Ragupathy, Synthesis and investigation on synergetic effect of activated carbon loaded silver nanoparticles with enhanced photocatalytic and antibacterial activities, *Environ. Res.*, 2023, **233**, 116431, DOI: 10.1016/j.envres.2023.116431.

14 D. Thirumoolan, S. Ragupathy, S. Renukadevi, P. Rajkumar, R. S. Rai, R. M. Saravana Kumarf, I. Hasan, M. Durai and Y. Ho Ahn, Influence of nickel doping and cotton stalk activated carbon loading on structural, optical, and photocatalytic properties of zinc oxide nanoparticles, *J. Photochem. Photobiol., A*, 2024, **448**, 115300, DOI: 10.1016/j.jphotochem.2023.115300.

15 M. Geetha, S. Renukadevi, D. Senthil Kumar, *et al.*, Efficient photocatalytic degradation of rhodamine B using Ag-doped TiO_2-loaded groundnut shell activated carbon under solar light, *Ionics*, 2024, **30**, 1167–1176, DOI: 10.1007/s11581-023-05344-w.

16 J. Y. Tang, R. T. Guo, W. G. Pan, W. G. Zhou and C. Y. Huang, Visible light activated photocatalytic behaviour of Eu (III) modified g-C_3N_4 for CO_2 reduction and H_2 evolution, *Appl. Surf. Sci.*, 2019, **467**, 206–212, DOI: 10.1016/j.apsusc.2018.10.143.

17 K. X. Zhu, Y. Lv, J. Liu, W. J. Wang, C. P. Wang, P. Wang, A. Meng, Z. J. Li and Q. D. Li, Explosive thermal exfoliation of intercalated graphitic carbon nitride for enhanced photocatalytic degradation properties, *Ceram. Int.*, 2019, **45**, 3643–3647, DOI: 10.1016/j.ceramint.2018.11.025.

18 J. Feng, M. M. Gao, Z. Q. Zhang, M. Z. Gu, J. X. Wang, W. J. Zeng and Y. M. Ren, Comparing the photocatalytic properties of g-C3N4 treated by thermal decomposition, solvothermal and protonation, *Results Phys.*, 2018, **11**, 331–334, DOI: 10.1016/j.rinp.2018.09.014.

19 C. Y. Liu, H. W. Huang, W. Cui, F. Dong and Y. H. Zhang, Band structure engineering and efficient charge transport in oxygen substituted g-C3N4 for superior photocatalytic hydrogen evolution, *Appl. Catal., B*, 2018, **230**, 115–124, DOI: 10.1016/j.apcatb.2018.02.038.

20 C. Ji Li, Y. Lu, L. Wu, S. Sun, R. Qu, C. Sun, Y. Zhang and Z. Xue, In situ synthesis of carbon/g-C_3N_4 composites for visible light catalysis by facile one-step pyrolysis of partially formaldehyde-modified dicyandiamide, *Mater. Chem. Phys.*, 2018, **214**, 28–33, DOI: 10.1016/j.matchemphys.2018.04.064.

21 M. Mitra, A. Habibi-Yangjeh and S. Rahim Pouran, Review on magnetically separable graphitic carbon nitride-based nanocomposites as promising visible-light-driven photocatalysts, *J. Mater. Sci. Mater. Electron.*, 2018, **29**, 1719–1747, DOI: 10.1007/s10854-017-8166-x.

22 H. He, J. Li, C. Yu and Z. Luo, Surface decoration of microdisk-like g-C_3N_4/diatomite with Ag/AgCl nanoparticles for application in Cr(VI) reduction, *Sustain. Mater. Technol.*, 2019, **22**, e00127, DOI: 10.1016/j.susmat.2019.e00127.

23 H. He, Z. Luo and C. Yu, Diatomite-anchored g-C_3N_4 nanosheets for selective removal of organic dyes, *J. Alloys Compd.*, 2020, **816**, 152652, DOI: 10.1016/j.jallcom.2019.152652.

24 W. Zhong, W. Tu, S. Feng and A. Xu, Photocatalytic H2 evolution on CdS nanoparticles by loading Fe Se nanorods as co-catalyst under visible light irradiation, *J. Alloys Compd.*, 2019, **772**, 669–674, DOI: 10.1016/j.jallcom.2018.09.145.

25 Xi chen, B. Zhou, S. Yang, H. Wu, Y. Wu, L. Wu, J. Pan and X. Xiong, In situ construction of an SnO_2/g-C_3N_4 heterojunction for enhanced visible-light photocatalytic activity, *RSC Adv.*, 2015, **5**, 68953–68963, DOI: 10.1039/C5RA11801H.

26 H. Gao, F. Wang, S. Wang, X. Wang, Z. Yi and H. Yang, Photocatalytic activity tuning in novel Ag_2S/CQDs/$CuBi_2O_4$ composite: Synthesis and photocatalytic mechanism, *Mater. Res. Bull.*, 2019, **115**, 140–149, DOI: 10.1016/j.materresbull.2019.03.021.

27 J. Jayachandiran, J. Yesuraj, M. Arivanandhan, B. Muthuraaman, R. Jayavel and D. Nedumaran, Bifunctional investigation of ultra-small SnO_2 nanoparticle decorated rGO for ozone sensing and supercapacitor

applications, *RSC Adv.*, 2021, **11**, 856–866, DOI: 10.1039/D0RA10137K.

28 H. Shen, X. R. Zhao, L. B. Duan, R. D. Liu and H. Li, Enhanced visible light photocatalytic activity in SnO_2@g-C_3N_4 core-shell structures, *Mater. Sci. Eng.*, 2017, **218**, 23–30, DOI: 10.1016/j.mseb.2017.01.006.

29 M. Jourshabani, Z. Shariatinia and A. Badiei, In situ fabrication of SnO2/S-doped g-C3N4 nanocomposites and improved visible light driven photodegradation of methylene blue, *J. Mol. Liq.*, 2017, **248**, 688–702, DOI: 10.1016/j.molliq.2017.10.110.

30 P. Praus, L. Svoboda, R. Dvorský and M. Reli, Nanocomposites of SnO_2 and g-C_3N_4: Preparation, characterization and photocatalysis under visible LED irradiation, *Ceram. Int.*, 2018, **44**, 3837–3846, DOI: 10.1016/j.ceramint.2017.11.170.

31 A. Akhundi and A. H. Yangjeh, A simple large-scale method for preparation of g-C_3N_4/SnO_2 nanocomposite as visible-light-driven photocatalyst for degradation of an organic pollutant, *Mater. Express*, 2015, **5**, 309–318, DOI: 10.1166/mex.2015.1242.

32 G. D. Bittner, C. Z. Yang and M. A. Stoner, Estrogenic chemicals often leach from BPA-free plastic products that are replacements for BPA-containing polycarbonate products, *Environ. Health*, 2014, **13**, 41, DOI: 10.1186/1476-069X-13-41.

33 A. Schecter, N. Malik, D. Haffner, S. Smith, T. Robert Harris, O. Paepke and L. Birnbaum, Bisphenol A (BPA) in U.S. Food, *Environ. Sci. Technol.*, 2010, **44**, 9425–9430, DOI: 10.1021/es102785d.

34 X. Dong, B. Ren, Z. Sun, C. Li, X. Zhang, M. Kong, S. Zheng and D. D. Dionysiou, Monodispersed $CuFe_2O_4$ nanoparticles anchored on natural kaolinite as highly efficient peroxymonosulfate catalyst for bisphenol A degradation, *Appl. Catal., B*, 2019, **253**, 206–217, DOI: 10.1016/j.apcatb.2019.04.052.

35 Y. Zhang, D. Zhang, L. Zhou, Y. Zhao, J. Chen, Z. Chen and F. Wang, Polypyrrole/reduced graphene oxide aerogel particle electrodes for high-efficiency electro-catalytic synergistic removal of Cr(VI) and bisphenol A, *Chem. Eng. J.*, 2018, **336**, 690–700, DOI: 10.1016/j.cej.2017.11.109.

36 S. Hossein Rajabnejad, H. Badibostan, A. Verdian, G. Reza Karimi, E. Fooladi and J. Feizy, Aptasensors as promising new tools in bisphenol A detection-an invisible pollution in food and environment, *Microchem. J.*, 2020, **155**, 104722, DOI: 10.1016/j.microc.2020.104722.

37 L. Ju, P. Wu, Q. Yang, Z. Ahmed and N. Zhu, Synthesis of ZnAlTi-LDO supported C60@AgCl nanoparticles and their photocatalytic activity for photo-degradation of Bisphenol A, *Appl. Catal., B*, 2018, **224**, 159–174, DOI: 10.1016/j.apcatb.2017.10.056.

38 J. Cao, C. Qin, Y. Wang, B. Zhang, Y. Gong, H. Zhang, G. Sun, H. Bala and Z. Zhang, Calcination Method Synthesis of SnO_2/g-C_3N_4 Composites for a High-Performance Ethanol Gas Sensing Application, *Nanomaterials*, 2017, **7**, 98, DOI: 10.3390/nano7050098.

39 L. Huang, F. Zhang, li Yeping, D. Penghui, Li Pengpeng, H. Xu and Li Huaming, Partial Oxidation of Sn^{2+} Induced Oxygen Vacancy Overspread on the Surface of SnO_{2-x}/g-C_3N_4 Composites for Enhanced LED-Light-Driven Photoactivity, *J. Inorg. Organomet. Polym. Mater.*, 2019, **29**, 765–775, DOI: 10.1007/s10904-018-1050-1.

40 P. More, S. Kadam, P. Lokhande, G. Jangam, S. Patange and D. Satpute, Effect of sintering temperature on the structural, morphological, and the magnetic properties of $Ni_{0.25}Cu_{0.55}Zn_{0.20}Fe_2O_4$ nano ferrite, *J. Magn. Magn. Mater.*, 2023, **586**, 171192, DOI: 10.1016/j.jmmm.2023.171192.

41 A. Kar, S. Kundu and A. Patra, Surface Defect-Related Luminescence Properties of SnO2 Nanorods and Nanoparticles, *J. Phys. Chem. C*, 2011, **115**, 118–124, DOI: 10.1021/jp110313b.

42 S. W. Hu, L. W. Yang, Y. Tian, X. L. Wei, J. W. Ding, J. X. Zhong and P. K. Chu, Simultaneous nanostructure and heterojunction engineering of graphitic carbon nitride *via in situ* Ag doping for enhanced photoelectrochemical activity, *Appl. Catal., B*, 2015, **163**, 611–622, DOI: 10.1016/j.apcatb.2014.08.023.

43 S. Liu, J. Ke, H. Sun, J. Liu, M. O. Tade and S. Wang, Size dependence of uniformed carbon spheres in promoting graphitic carbon nitride toward enhanced photocatalysis, *Appl. Catal., B*, 2017, **204**, 358–364, DOI: 10.1016/j.apcatb.2016.11.048.

44 Y. R. Girish, B. R. Udayabhanu, N. M. Byrappa, G. Alnaggar, A. Hezam, G. Nagaraju, K. Pramoda and K. Byrappa, Rapid and facile synthesis of Z-scheme ZnO/g-C_3N_4 heterostructure as efficient visible light-driven photocatalysts for dye degradation and hydrogen evolution reaction, *J. Hazard. Mater. Adv.*, 2023, **9**, 100230, DOI: 10.1016/j.hazadv.2023.100230.

45 D. Pradhan, L. Mohanty, R. Singhal, E. Falletta and S. K. Dash, Sustainable and solar light assisted photocatalytic degradation of MB and MG dyes by Co_3O_4/g-C_3N_4 nanocomposite, *Inorg. Chem. Commun.*, 2023, **156**, 111259, DOI: 10.1016/j.inoche.2023.111259.

46 G. R. Surikanti, P. Bajaj and M. V. Sunkara, g-C_3N_4-Mediated Synthesis of Cu_2O to Obtain Porous Composites with Improved Visible Light Photocatalytic Degradation of Organic Dyes, *ACS Omega*, 2019, **4**, 17301–17316, DOI: 10.1021/acsomega.9b02031.

47 D. T. N. Hoa, N. T. T. Tu, H. Q. A. Thinh, L. Van Thanh Son, L. V. T. Son, N. D. V. Quyen, L. L. Son, T. N. Tuyen, P. L. M. Thong, L. H. Diem and D. Q. Khieu, TiO_2/g-C3N4 Visible-Light-Driven Photocatalyst for Methylene Blue Decomposition, *J. Nanomater.*, 2023, 9967890, DOI: 10.1155/2023/9967890.

48 H. Yang, Z. Jin, H. Hu, Y. Bi and G. Lu, Ni-Mo-S nanoparticles modified graphitic C_3N_4 for efficient hydrogen evolution, *Appl. Surf. Sci.*, 2018, **427**, 587–597, DOI: 10.1016/j.apsusc.2017.09.021.

49 A. Ran, B. Dlugatch, M. S. Chae, Y. Goffer and D. Aurbach, Changes in the interfacial charge-transfer resistance of Mg metal electrodes, measured by dynamic electrochemical

impedance spectroscopy, *Electrochem. Commun.*, 2021, **124**, 106952, DOI: 10.1016/j.elecom.2021.106952.

50 W. Choi, H. Shin, J. Kim, J. Choi and W. Yoon, Modeling and Applications of Electrochemical Impedance Spectroscopy (EIS) for Lithium-ion Batteries, *J. Electrochem. Sci. Technol.*, 2020, **11**(1), 1–13, DOI: 10.33961/jecst.2019.00528.

51 F. Chang, Y. Lei, J. Li, S. Li, D. G. Liu and Y. Kong, Externally modified Bi12SiO20 with BiOI: np heterojunctions for effectually photocatalytic degradation of bisphenol A, *Sep. Purif. Technol.*, 2023, **323**, 124516, DOI: 10.1016/j.seppur.2023.124516.

52 F. Chang, J. Li, Y. Kou, W. Bao, Z. Shi, G. Zhu and Y. Kong, The intense charge migration and efficient photocatalytic NO removal of the S-scheme heterojunction composites $Bi_7O_9I_3$-BiOBr, *Sep. Purif. Technol.*, 2025, **353**, 128402, DOI: 10.1016/j.seppur.2024.128402.

53 C. Harak, D. Satpute, V. Kadam, N. Kolhe, A. Wade, S. Balgude, S. Mardikar, S. Balgude and H. Pawar, Morphology controlled fabrication of Fe_2O_3/GCN composites: a comparative study of hydrothermal and sonochemical synthesis methods for efficient sunlight driven photocatalysis for environmental remediation, *Emergent Mater.*, 2023, **6**, 1797–1807, DOI: 10.1007/s42247-023-00566-0.

54 Y. He, L. Zhang, M. Fan, X. Wang, M. L. Walbridge, Q. Nong, Y. Wu and L. Zhao, Z-scheme SnO_{2-x}/g-C3N4 composite as an efficient photocatalyst for dye degradation and photocatalytic CO_2 reduction, *Sol. Energy Mater. Sol. Cell.*, 2015, **137**, 175–184, DOI: 10.1016/j.solmat.2015.01.037.

55 B. Zhu, P. Xia, Y. Li, W. Ho and J. Yu, Fabrication and photocatalytic activity enhanced mechanism of direct Z-scheme g-C3N4/Ag2WO4 photocatalyst, *Appl. Surf. Sci.*, 2017, **391**, 175–183, DOI: 10.1016/j.apsusc.2016.07.104.

56 S. Arade, P. Agale, S. Balgude, S. Patange, D. Hingane and P. More, Zn0. 5Ni0. 5MnxFe2-xO4 magnetically separable nano ferrite: A highly efficient photocatalyst for environmental remediation, *Inorg. Chem. Commun.*, 2024, **170**, 113170, DOI: 10.1016/j.inoche.2024.113170.

57 C. Tan, L. Ai, L. Wang, M. Xu, N. Guo, D. Jia, L. Feng, M. Lu and X. Zhang, BiOCl Nanosheets with Vacancy Containing (001) and (110) Facets for the Photocatalytic Degradation of Organic Contaminants, *ACS Appl. Nano Mater.*, 2023, **6**, 21216–21225, DOI: 10.1021/acsanm.3c04327.

58 Y. Zhang, W. Li, Z. Hu, X. Jing and L. Yu, Mo@PANI-catalyzed oxidative deoximation reaction, *Chin. Chem. Lett.*, 2024, **35**(2), 108938, DOI: 10.1016/j.cclet.2023.108938.

59 D. Li, J. Huang, R. Li, P. Chen, D. Chen, M. Cai, H. Liu, Y. Feng, W. Lv and G. Liu, Synthesis of a carbon dots modified g-C_3N_4/SnO_2 Z-scheme photocatalyst with superior photocatalytic activity for PPCPs degradation under visible light irradiation, *J. Hazard. Mater.*, 2021, **401**, 123257, DOI: 10.1016/j.jhazmat.2020.123257.

60 A. Fazli, S. Lauciello, R. Brescia, R. Carzino, A. Athanassiou and D. Fragouli, Synergistic degradation of polystyrene nanoplastics in water: Harnessing solar and water-driven energy through a Z-scheme SnO_2/g-C_3N_4/PVDF-HFP piezo-photocatalytic system, *Applied Catalysis B: Environment and Energy*, 2024, **353**, 124056, DOI: 10.1016/j.apcatb.2024.124056.

61 A. Mohammad, M. E. Khan, MdR. Karim and M. H. Cho, Synergistically effective and highly visible light responsive SnO_2-g-C_3N_4 nanostructures for improved photocatalytic and photoelectrochemical performance, *Appl. Surf. Sci.*, 2019, **495**, 143432, DOI: 10.1016/j.apsusc.2019.07.174.

62 X. Wang and P. Ren, Flower-like SnO2/g-C3N4 heterojunctions: The face-to-face contact interface and improved photocatalytic properties, *Adv. Powder Technol.*, 2018, 1153–1157, DOI: 10.1016/j.apt.2018.02.006.

63 X. Wang, Y. He, L. Xu, Yi Xia and R. Gang, SnO_2 particles as efficient photocatalysts for organic dye degradation grown in-situ on g-C3N4 nanosheets by microwave-assisted hydrothermal method, *Mater. Sci. Semicond. Process.*, 2021, **121**, 105298, DOI: 10.1016/j.mssp.2020.105298.

64 H. Shen, X. Zhao, L. Duan, R. Liu and H. Li, Enhanced visible light photocatalytic activity in SnO2@g-C3N4 core-shell structures, *Mater. Sci. Eng. B*, 2017, **218**, 23–30, DOI: 10.1016/j.mseb.2017.01.006.

65 B. Babu, M. Cho, C. Byon and J. Shim, Sunlight-driven photocatalytic activity of SnO2 QDs-g-C3N4 nanolayers, *Mater. Lett.*, 2018, **212**, 327–331, DOI: 10.1016/j.matlet.2017.10.110.

66 T. Zhang, F. Chan, Y. Qi, X. Zhang, J. Yang, X. Liu and S. Li, A facile one-pot and alkali-free synthetic procedure for binary SnO2/g-C3N4 composites with enhanced photocatalytic behaviour, *Mater. Sci. Semicond. Process.*, 2020, **115**, 105112, DOI: 10.1016/j.mssp.2020.105112.

67 K. Preethi Kirubakaran, S. Thangavel, G. Nallamuthu, V. Vasudevan, P. A. S. Ramasubramanian, A. Kumar and G. Venugopal, Enhanced Photocatalytic Degradation Activity of 2-D Graphitic Carbon Nitride-SnO_2, *Nanohybrids*, 2019, **19**, 3576–3582, DOI: 10.1166/jnn.2019.16033.